5-2019

CFD Study of Taylor-Like Vortices in Swirling Flows

Sattar Panahandehgar

CFD STUDY OF TAYLOR-LIKE VORTICES IN SWIRLING FLOWS

A Thesis

Submitted to the Faculty

of

Embry-Riddle Aeronautical University

by

Sattar Panahandehgar

In Partial Fulfillment of the

Requirements for the Degree

of

Master of Science in Aerospace Engineering

May 2019

Embry-Riddle Aeronautical University

Daytona Beach, Florida

CFD STUDY OF TAYLOR-LIKE VORTICES
IN SWIRLING FLOWS

by

Sattar Panahandehgar

A Thesis prepared under the direction of the candidate's committee chairman, Dr. Yechiel Crispin, Department of Aerospace Engineering, and has been approved by the members of the thesis committee. It was submitted to the School of Graduate Studies and Research and was accepted in partial fulfillment of the requirements for the degree of Master of Science in Aerospace Engineering.

THESIS COMMITTEE

Chairman, Dr. Yechiel Crispin

Member, Dr. Eric Perrell

Member, Dr. Mark Ricklick

Graduate Program Coordinator, Dr. Magdy Attia — Date 4/23/2019

Dean of College of Engineering, Dr. Maj Mirmirani — Date 4/24/2019

Senior Vice President for Academic Affairs and Provost, Dr. Lon Moeller — Date 4/24/19

ACKNOWLEDGMENTS

Firstly, I want to give special thanks to my advisor Dr. Yechiel Crispin for his guidance and infinite support throughout the past two years. I have an immense appreciation for his intellect and counseling during my research. Second, I would like to thank Dr. Eric Perrell and Dr. Mark Ricklick for their insight as thesis committee members. I would also like to acknowledge all my professors and faculty members of the Department of Aerospace Engineering at Embry-Riddle Aeronautical University. Distinctly, I want to recognize the program coordinator Dr. Magdy Attia for his continuous aid and support. Further, I want to thank Eagle Flight Research Center and Dr. Pat Anderson for the research opportunity and assistance. Lastly, I am especially grateful to my family and Bridget Pounsberry, without whom, I would not be able to accomplish my goals and aspirations at this stage of my life.

TABLE OF CONTENTS

LIST OF FIGURES v

SYMBOLS vii

ABBREVIATIONS viii

ABSTRACT ix

1. Introduction 1

1.1. The Importance of Swirling Flows 1
1.2. Industry Applications 2
1.3. Vortex Injection in Hybrid Rocket Engines 4
1.3.1. Mathematical Model 6
1.3.2. Literature Review 8
1.4. Thesis Layout 9

2. Problem Statement 10

3. Solution Method 12

3.1. Governing Equations 12
3.2. Axisymmetric Swirling Flow 14
3.3. Turbulence Modeling 17
3.4. CFD Software Set-Up 20

4. Results Analysis 22

4.1. 2D Incompressible Gas 22
4.1.1. 2D Incompressible Gas with RNG $\boldsymbol{k-\varepsilon}$ Turbulence Model 23
4.1.2. 2D Incompressible Gas with RSM Turbulence Model 28
4.2. 2D Incompressible Liquid 30
4.3. 3D Incompressible Gas 32
4.4. 2D Compressible Gas 36

5. Discussion of Findings 38

5.1. Swirl Number and Swirl Decay 38
5.2. Taylor-Like Vortices 41
5.2.1. Taylor-Couette Flow 41
5.2.2. Free-surface vortex flow 44

6. Summary and Conclusion 46

REFERENCES 47

A. Industrial Applications examples 50

B. Example of Highly Swirling Flow Turbulence Modeling. 53

LIST OF FIGURES

Figure 1. 1 Tornado (photograph courtesy Goddard B.). 1
Figure 1. 2 Von Kármán vortex (asknature.org) (David K.). 2
Figure 1. 3 Kelvin-Helmholtz Instability. 2
Figure 1. 4 Schematic of a vortex tube (Jeevahan et al., 2016). 3
Figure 1. 5 Bidirectional VIHRE (Chiaverini & Kuo, 2007). 5
Figure 1. 6 Injector Port Configuration (Roy & Frederick, 2016). 6
Figure 1. 7 VIHRE chamber Geometry (Halpenny & Majdalani, 2008)..... **7**
Figure 2. 1 Simple 3D cylindrical chamber geometry including a tangential inlet. 10
Figure 4. 1 2D axisymmetric structured mesh generated in Pointwise. 22
Figure 4. 2 Zoom in to the left end of the mesh shown in Figure 4.1. 23
Figure 4. 3 Tangential velocity at $x/l = 0.4$ (2D incompressible RNG $k-\varepsilon$) 24
Figure 4. 4 Axial velocity at $x/l = 0.4$ (2D incompressible RNG $k-\varepsilon$) 25
Figure 4. 5 Radial velocity at x/l=0.4 (2D incompressible RNG k-ε) 25
Figure 4. 6 Tangential velocity contour with a velocity-inlet of $\frac{u_\theta}{u_z} \lesssim 2.5$ 26
Figure 4. 7 Tangential velocity contour with a velocity-inlet of $\frac{u_\theta}{u_z} \approx 2.5$. 26
Figure 4. 8 Tangential velocity contour with a velocity-inlet of $\frac{u_\theta}{u_z} \gtrsim 2.5$ 27
Figure 4. 9 (a) Velocity vectors (u_z and u_r) colored by bulk velocity magnitude representing counter-rotating axisymmetric toroidal vortices. (b) Zoom in on the left-end and (c) further zoom on vortices. 28
Figure 4. 10 Tangential velocity at $x/l = 0.4$ (2D incompressible RSM). 29
Figure 4. 11 Axial velocity at x/l = 0.4 (2D incompressible RSM). 29
Figure 4. 12 (a) Velocity vectors (u_z and u_r) colored by bulk velocity magnitude representing counter-rotating axisymmetric toroidal vortices (2D incompressible RSM). (b) Zoom in on the left-end and (c) further zoom on vortices. 30
Figure 4. 13 Tangential velocity at $x/l = 0.4$ (2D Water). 31
Figure 4. 14 Axial velocity at $x/l = 0.4$ (2D Water). 31
Figure 4. 15 Radial velocity at $x/l = 0.4$ (2D Water). 32
Figure 4. 16 (a) The 3D structured axisymmetric grid generated in Pointwise and (b) zoom in view to one side of the cylinder. 32
Figure 4. 17 Velocity streamlines in the 3D case (Tecplot). 33
Figure 4. 18 Tangential velocity contour over a vertical cross-section of the 3D model. 34

Figure 4. 19 Tangential velocity contour over a horizontal cross-section at $xl = 0.4$ (3D case). 34

Figure 4. 20 Axial velocity contour over a horizontal cross-section at $xl = 0.4$ (3D case). 35

Figure 4. 21 Radial velocity contour over a horizontal cross-section at $xl = 0.4$ (3D case). 35

Figure 4. 22 Tangential velocity at $x/l = 0.4$ (2D compressible case). 36

Figure 4. 23 Axial velocity at $x/l = 0.4$ (2D compressible case). 36

Figure 4. 24 Radial velocity at $x/l = 0.4$ (2D compressible case). 37

Figure 5. 1 Relative Swirl number decay as a function of x/D. 39

Figure 5. 2 Relative Swirl number decay as a function of x/D for a range of Reynolds numbers (Von Lavante and Yao. (2012)). 40

Figure 5. 3 Relative Swirl number decay as a function of x/D(2D cases) 41

Figure 5. 4 Taylor-Couette flow system. 42

Figure 5. 5 Taylor vortices visualization (Moser et al., 2002). 44

Figure 5. 6 Free-surface vortex flow system with full virtual air core (Mulligan, 2015). 45

Figure A. 1 Lab-scale Gas turbine combustor (Hummel, 2016). 50

Figure A. 2 Industrial Swirl Burner (vbt.ebi.kit.edu). 51

Figure A. 3 Heavy-duty Cavex hydrocyclones (Weir Minerals). 51

Figure A. 4 Schematic of a Hydrocyclone (Ozgen & Yildiz, 2010). 52

Figure B. 1 Tangential velocity profile at a location below the vortex finder (Ansys, Inc. 2013). 53

SYMBOLS

k	turbulence kinetic energy
p	pressure
r	radial coordinate, radius
$\dot{q}$	rate of heat generation per unit volume
$\vec{u}$	velocity vector
u_r	radial velocity
u_z	axial velocity
u_θ	tangential velocity
z	axial coordinate
D	diameter
$D_{L,ij}$	molecular diffusion
D_{p_o}	initial diameter of the port
$D_{T,ij}$	turbulence diffusion
F	body forces
F_{ij}	production by system rotation
G_{ij}	buoyancy production
G_x	axial momentum flux
G_θ	angular momentum flux
L_p	port length
P_c	chamber pressure
P_{ij}	stress production
Re	Reynolds number
S	swirl number
T	Taylor number
T_c	critical Taylor number
T_c	chamber temperature
β	thermal expansion coefficient
γ	specific heat ratio
ε	turbulence dissipation rate
θ	tangential coordinate
μ	dynamic viscosity
μ_t	turbulence viscosity
ν	kinematic viscosity
ρ	density
τ	shear stress
Γ	circulation
ϕ_{ij}	pressure strain
Φ	viscous dissipation rate
Ω	angular velocity

ABBREVIATIONS

CFD	computational fluid dynamics
DNS	direct numerical simulation
RANS	Reynolds averaged Navier-Stokes equations
RSM	Reynolds stress model
RNG	renormalization group theory
VIHRE	vortex injection in hybrid rockets engines

ABSTRACT

Panahandehgar, Sattar MSAE, Embry-Riddle Aeronautical University, May 2019. CFD Study of Taylor-Like Vortices in Swirling Flows.

Swirling flows are complex fluid motions that appear in various natural phenomena and man-made devices. Numerous engineering applications such as turbomachinery, jet engine combustion chambers, mixing tanks and industrial burners involve swirling flows. This wide range of applications is due to unique characteristics offered by swirling flows such as increase in mixing rate, heat transfer rate and wall shear stress. In this study the axisymmetric swirling flow behavior in the context of a hybrid rocket engine have been analyzed. While modeling the flow inside a cylindrical chamber using CFD, a similarity with the Taylor vortices instability has been observed. Similar to the classic Taylor-Couette flow system, a secondary flow field in the form of wavy toroidal vortices spaced regularly along the axial direction appear under certain critical conditions. The dimensionless control parameter governing the formation of the Taylor-like vortices is expressed as the ratio of the tangential to axial velocity components.

1. Introduction

Swirling and vortex flows are complex fluid motions that appear in various natural phenomena and industrial fluid mechanics. Although these phenomena have been studied over the past few decades in different contexts, there are still numerous unanswered and unsolved problems related to swirling and vortex flows. This study mainly concentrates on the numerical (CFD) investigation of the swirling flow in the context of hybrid rocket engines; focusing on the existence of Taylor-like vortices under certain circumstances.

1.1. The Importance of Swirling Flows

In nature, swirling and vortex flows are predominately caused by density, velocity, and temperature differences between various layers of environmental fluid systems. The tornado (Figure1.1) is a good example of a natural swirling flow seen in nature. The wind shear and instabilities in lower atmosphere layers generate tornados.

Figure 1.1 Tornado (photograph courtesy Goddard B.)

Natural vortex flows such as Von Kármán vortex (Figure1.2) and Kelvin-Helmholtz Instability (Figure1.3) are other famous examples of this interesting fluid dynamics.

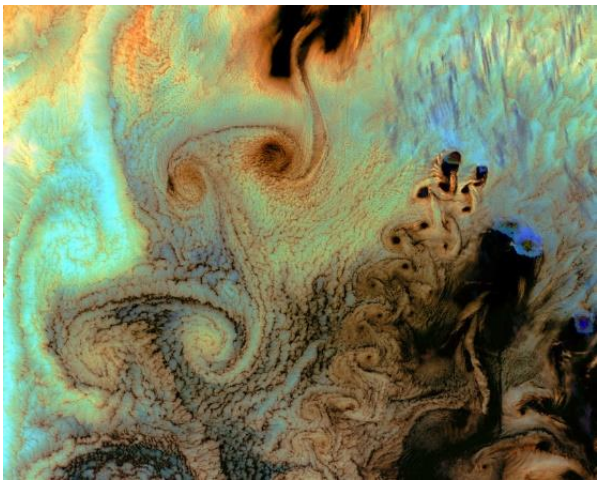

Figure 1.2 Von Kármán vortex (asknature.org) (David K.)

Figure 1.3 Kelvin-Helmholtz Instability

The importance of studying swirling and vortex flows is more significant when analyzing other catastrophic natural phenomena such as hurricanes. A deep knowledge and understanding of this type of fluid motion may result in saving millions of lives and prevent enormous financial losses. Besides all these natural phenomena, the concept of swirling flow is widely used in various industrial processes and man-made devices. In the following section, some insight in regards to the swirling flow within industry is given.

1.2. Industry Applications

Swirls and vortices are the main components of turbulence flow. Turbulence mixing

exists in many industrial fluid mechanic devices and it is one of the essential ingredients of numerous industrial processes. Besides mixing, increase in momentum and heat transfer are other results of swirling motion of the fluid. Swirling flows are very useful and essential in the industrial processes involving mixing, liquid-particle or liquid-liquid separation, and combustion stabilization.

For instance, swirling flow is the main operation principal of the Vortex tubes. Figure 1.4 represents a schematic of a vortex tube. As shown in the schematic, high-pressure gas is tangentially injected into the swirl chamber while accelerated and it is forced to swirl at a high rate. The presence of the conical nozzle at the aft-end of the tube allows only the escape of the outer layer of the compressed gas. The part of the gas that is not able to exit is forced to return within the outer flow creating a swirl flow. The inner flow loses energy, cools down, and at the same time, outer flow gains this energy. This device is very useful in cooling of cutting tools in machining shops.

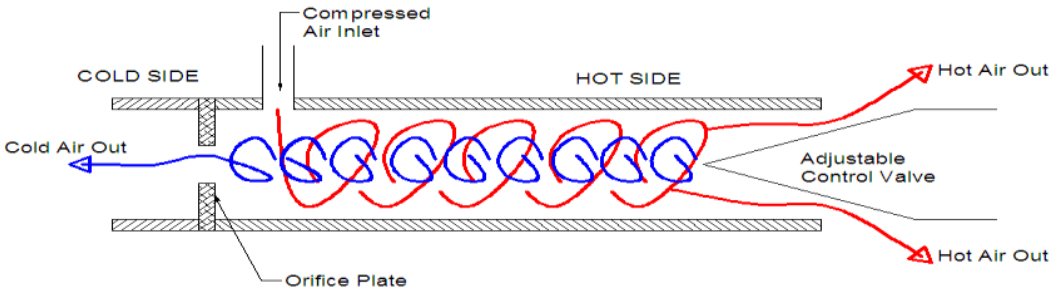

Figure 1.4 Schematic of a vortex tube (Jeevahan et al., 2016)

Other applications of swirling flows are found in gas turbine combustors, industrial swirl burners, hydrocyclones, etc. In the first two, swirling flows are essential for flame and combustion stabilization and increase in mixing and heat exchange rate. Hydrocyclones are utilized for separation of the particles suspended in liquids. They can

also separate two liquids of different densities. A schematic of each of these examples is found in the Appendix A.

1.3. Vortex Injection in Hybrid Rocket Engines

Hybrid rockets are known for two major benefits: safety and simplicity compared to other types of rockets. Its separate storage of the fuel and the oxidizer increases the overall safety and reliability of the system. In addition, hybrids are chemically simpler than solid rockets and mechanically simpler than liquid rockets. However, three principal deficiencies have been observed in Hybrid Rocket Engines which keep them unpopular compared to solid rocket motors. These deficiencies include poor regression rate, low combustion efficiency and low volumetric loading, resulting in slow diffusion flames along the boundary between the gaseous oxidizer and solid fuel surface. All these factors combined result in a lower applicability of hybrid rockets in industries.

Increasing the regression rate three to four times is a possible solution to overcome this problem (Chiaverini & Kuo, 2007). The Vortex Injection in Hybrid Rocket Engines (VIHRE) grants up to seven times an increase in the regression rate compared to the classical injection systems in hybrids. Figure 1.5 shows a schematic of a VIHRE.

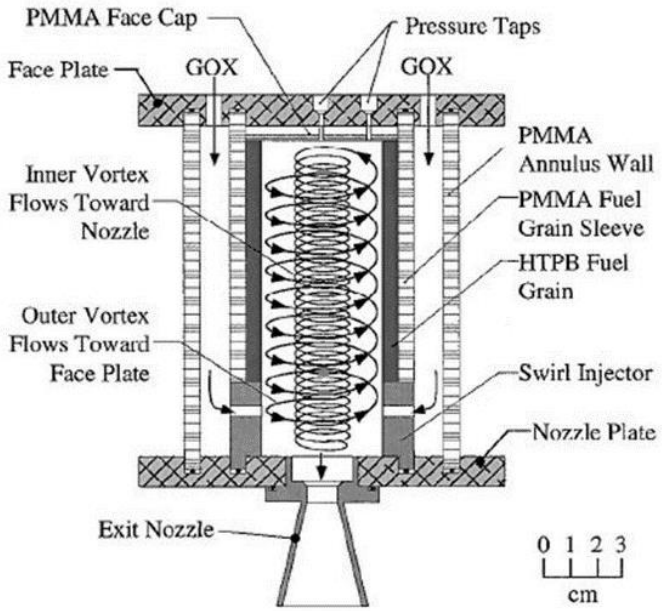

Figure 1.5 Bidirectional VIHRE (Chiaverini & Kuo, 2007).

A vortex injector has been placed at the aft edge of the engine just before the nozzle, which generates a pair of coaxial and counter-flowing swirls. As a result, high turbulence flow of the oxidizer aids in mixing and increases notably the surface erosion. Figure 1.6 represents the vortex injector itself where the ports are aligned tangentially with the inner circumference, forcing the flow to produce a vortex. The generated strong vortex moves helically from the aft-end toward the head over the fuel surface. The fuel-oxidizer mixture is compelled to spiral around the axis of the chamber and crossing the chamber length twice before exiting. Consequently, regression rate and over all combustion efficiency are improved due to the increased residence time and intense mixing of the fuel and oxidizer.

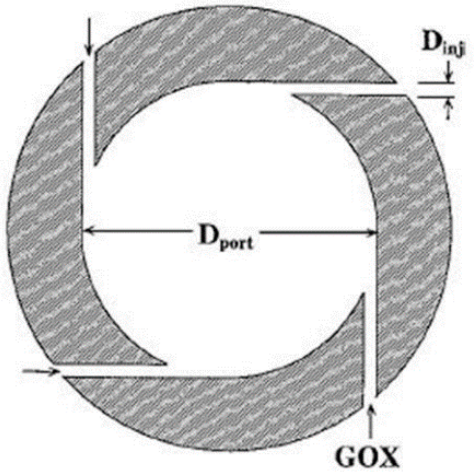

Figure 1.6 Injector Port Configuration (Roy & Frederick, 2016).

Another important feature of VIHRE is the use of hollow cylindrical cartridges, which results in a reduction of overall volumetric loading and case housing costs.

After analyzing the actual concept of VIHRE, the theoretical mathematical model can be applied on the core flow. This gives a better understanding of the mean flow motion and behavior inside the engine.

1.3.1. Mathematical Model

The geometry of the cylindrical chamber of a VIHRE in presence of the bidirectional vortex is represented in Figure 1.7. In this schematic L_0 is the porous length and a is the radius of the cylinder, and downstream is partially open and attached to the nozzle with the radius of *b*. The radial and axial coordinates are donated by *r* and *z* respectively.

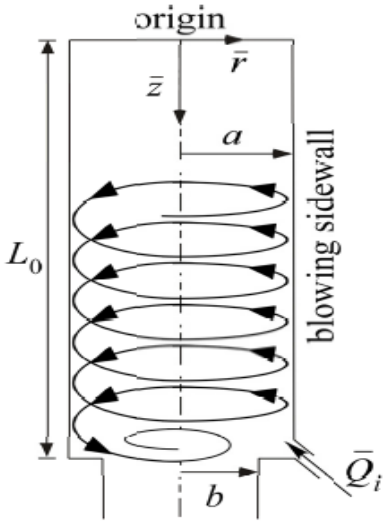

Figure 1.7 VIHRE chamber Geometry (Halpenny & Majdalani, 2008).

A cold-flow model is considered in order to characterize the mean gas motion. The flow is assumed steady, inviscid, incompressible, rotational, and axisymmetric. In absence of friction between the flow and the walls and based on these assumptions, Euler's equation are given as follow (Majdalani & Vyas, 2004):

$$\frac{1}{\bar{r}}\frac{\partial(\overline{ru_r})}{\partial r} + \frac{\partial \overline{u_z}}{\partial z} = 0 \tag{1.1}$$

$$\overline{u_r}\frac{\partial \overline{u_r}}{\partial r} + \overline{u_z}\frac{\partial \overline{u_r}}{\partial z} - \frac{\overline{u_\theta}^2}{\bar{r}} = -\frac{1}{\rho}\frac{\partial \overline{p}}{\partial r} \tag{1.2}$$

$$\overline{u_r}\frac{\partial \overline{u_\theta}}{\partial r} + \frac{\overline{u_\theta}\,\overline{u_r}}{\partial z} = 0 \tag{1.3}$$

$$\overline{u_r}\frac{\partial \overline{u_z}}{\partial r} + \overline{u_z}\frac{\partial \overline{u_z}}{\partial z} = -\frac{1}{\rho}\frac{\partial \overline{p}}{\partial z} \tag{1.4}$$

Further details regarding the required boundary conditions and the Euler-type solution can be found in chapter 6 of the book by Chiaverini & Kuo (2007). Correspondingly, the viscous corrections can be solved in both axial and radial direction.

1.3.2. Literature Review

The improvement in regression rate and combustion efficiencies in VIHRE have been demonstrated by several experiments and ground or flight tests. In fact, many studies are limited to analyzing the effect of swirling injection of the gaseous oxidizer on the rocket's performances. Generally, researches and studies on the topic of the VIHRE can be divided into the following four main groups:

First, publications that focus on the theoretical aspect of the mean flow motion in the VIHRE. Mainly, an approximate solution of the governing equations is provided and fundamental flow characteristics are illustrated. However, neglecting important factors such as effects of heat transfer and compressibility make the solutions nonrealistic (Chiaverini & Kuo, 2007), (Majdalani et al., 2004), and (Yoshimura & Sawada, 2010).

Second, works that compare the pure axial oxidizer injection with vortex oxidizer injection hybrid rocket. Based on results of these types of studies, fuel surface regression rate in the VIHRE can increase up to 50% compared to the non-swirling injection method. Additionally, overall efficiencies of the hybrid rocket can improve up to 20% by using vortex injection method (Bellomo et al., 2011) and (Jones et al., 2009).

Third, the studies that include the comparison between analytical and experimental data. Experimental data are extracted from a ground test. By comparing the data, some inconsistencies have been observed, which could be due to assumptions made while obtaining the analytical results (Myre et al, 2010),(Wongyai & Greatrix, 2015), and

(Arena et al., 2011).

Fourth, investigations on the configuration of the vortex generators. As mentioned before the advantages of vortex injection have been demonstrated experimentally. However, the mechanism of the injectors has not been completely clarified. Correspondingly, numerous researches are conducted in order to establish the most efficient way of this type of injection. For instance, different configuration of the injector ports have been examined (Motoe & Shimada, 2009), (Marquart et al., 2015), (Paccagnella & Karabeyoglu et al., 2015), (Ohyama et al., 2012), and (Tada et al.2002).

The simplifying physical assumptions limit the applicability of the results obtained in previous research. Most of the past and current research assumes the bulk gas motion in the chamber to be incompressible, no heat transfer, steady and inviscid (however, some viscous corrections were added to the results).

1.4. Thesis Layout

This thesis is organized in 6 chapters and 2 Appendices. The second chapter includes the problem statement. In chapter 3 the solution methodology is introduced. This chapter also includes the governing equations and an adapted strategy to solve the problem. At the end of chapter 3 a detailed description of the CFD program set up is outlined. Chapter 4 and 5 provide the obtained results and discussion for each individual computed case. Finally, in chapter 6 a summary of the findings is presented followed by an overall conclusion and future research avenues.

2. Problem Statement

The initial objective of this thesis was to model and analyze the effects of swirling injection of the oxidizer on the combustion process of a hybrid rocket. In order to accomplish this objective a simple model of the combustion chamber has been designed. Figure 2.1 represents a simple CAD model of a cylindrical chamber. In this geometry, the swirling flow is generated by tangentially injecting the oxidizer trough a single inlet. It is worth noting, various other inlet configurations can be designed as the swirl generator. For instance, instead of using just one inlet as shown in figure 2.1, 4 symmetric inlets can be used.

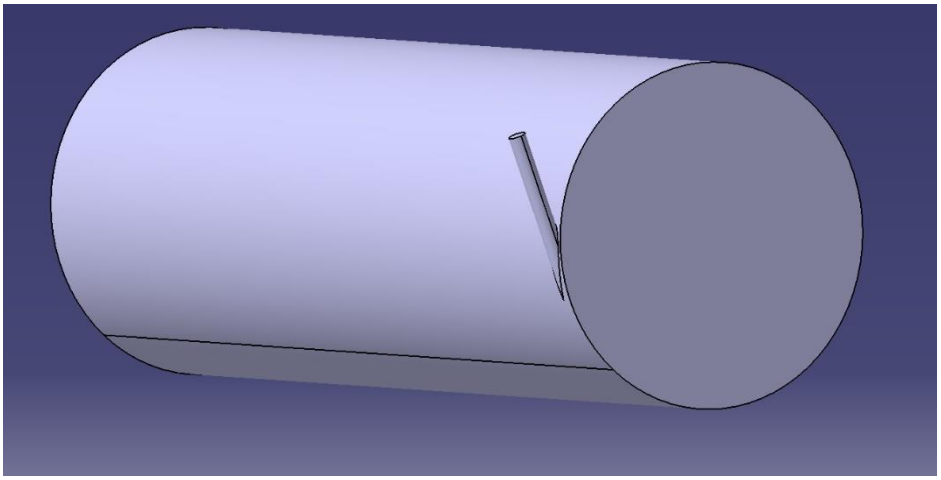

Figure 2.1 Simple 3D cylindrical chamber geometry including a tangential inlet.

The swirling flow can be obtained through boundary conditions at one end of the main cylinder. A detailed discussion on the boundary conditions and swirl production is provided in the following chapters.

The numerical model is based on sizing of a hybrid rocket for Space Ship One. The geometry and dimensions are obtained based on estimated data from the preliminary

design and the mission of the vehicle. Dimensions of one port out of 7 total ports of the hybrid rocket are found as the port initial diameter $D_{p_o} = 0.1\ m$ and the port length $L_p = 1.4\ m$ (aspect ratio of 14). These dimensions are mainly used in the mesh generating for the CFD analysis. However, the effect of aspect ratio on the results is analyze by changing the length size.

Considering the operating conditions of the hybrid rocket for Space Ship One, the flow speed is approximated as $V = 134\ m/s$. It is assumed that an oxidizer gas such as N_2O_4 is injected into the cylindrical port with a swirling motion. During the combustion process, a solid fuel ($HTPB$) is reacting with the oxidizer at an $O/F = 3.12$. The mass flow rate for one port is given $\dot{m} = 3.4\ kg/s$ .The specific heat ratio is $\gamma = 1.235$. The pressure and temperature of the chamber are given as $P_c = 3.7\ MPa$ and $T_c = 3350\ K$ respectively. The density of the mixture is estimated as $\rho = 3.25\ kg/m^3$ and the viscosity as $\mu = 8.17\ kg/ms$.The given data have been used to estimate the bulk flow's Reynolds number as $Re \approx 5 \times 10^5$.

The actual analysis of the sizing of a hybrid rocket is found in the literature (Larson et al., 1995).

3. Solution Method

This chapter provides the equations governing the swirling flow in a cylinder and the simplifying assumptions. Section 3.3 describes turbulence modeling as an important aspect of solving swirling flows. Finally, the CFD software set-up is provided.

3.1. Governing Equations

The governing equations are the Navier-Stokes equation in cylindrical coordinates:

r -momentum:

$$\rho\left[\frac{\partial u_r}{\partial t}+u_r\frac{\partial u_r}{\partial r}+\frac{u_\theta}{r}\frac{\partial u_r}{\partial \theta}+u_z\frac{\partial u_r}{\partial z}-\frac{u_\theta u_\theta}{r}\right] = -\frac{\partial p}{\partial r}-\left(\frac{1}{r}\frac{\partial}{\partial r}(r\tau_{rr})+\frac{1}{r}\frac{\partial \tau_{r\theta}}{\partial \theta}-\frac{\tau_{\theta\theta}}{r}+\frac{\partial \tau_{rz}}{\partial z}\right)+F_r \tag{3.1}$$

θ-momentum:

$$\rho\left[\frac{\partial u_\theta}{\partial t}+u_r\frac{\partial u_\theta}{\partial r}+\frac{u_\theta}{r}\frac{\partial u_\theta}{\partial \theta}+u_z\frac{\partial u_\theta}{\partial \theta}+\frac{u_\theta u_r}{r}\right] = -\frac{1}{r}\frac{\partial p}{\partial \theta}-\left(\frac{1}{r^2}\frac{\partial}{\partial r}(r^2\tau_{r\theta})+\frac{1}{r}\frac{\partial \tau_{\theta\theta}}{\partial \theta}+\frac{\partial \tau_{\theta z}}{\partial z}\right)+F_\theta \tag{3.2}$$

z-momentum:

$$\rho\left[\frac{\partial u_z}{\partial t}+u_r\frac{\partial u_z}{\partial r}+\frac{u_\theta}{r}\frac{\partial u_z}{\partial \theta}+u_z\frac{\partial u_z}{\partial z}\right] = -\frac{\partial p}{\partial z}-\left(\frac{1}{r}\frac{\partial}{\partial r}(r\tau_{rz})+\frac{1}{r}\frac{\partial \tau_{\theta z}}{\partial \theta}+\frac{\partial \tau_{zz}}{\partial z}\right)+F_z \tag{3.3}$$

In these equations, the shear stress constitutive equations are given as follow:

$$\tau_{rr} = -\mu\left[2\frac{\partial u_r}{\partial r} - \frac{2}{3}(\nabla.\vec{u})\right] \tag{3.4}$$

$$\tau_{\theta\theta} = -\mu\left[2(\frac{1}{r}\frac{\partial u_\theta}{\partial \theta} + \frac{u_r}{r}) - \frac{2}{3}(\nabla.\vec{u})\right] \tag{3.5}$$

$$\tau_{zz} = -\mu\left[2\frac{\partial u_z}{\partial z} - \frac{2}{3}(\nabla.\vec{u})\right] \tag{3.6}$$

$$\tau_{r\theta} = \tau_{\theta r} = -\mu\left[r\frac{\partial}{\partial r}\left(\frac{u_\theta}{r}\right) + \frac{1}{r}\frac{\partial u_r}{\partial \theta}\right] \tag{3.7}$$

$$\tau_{rz} = \tau_{zr} = -\mu\left[2\frac{\partial u_z}{\partial r} + \frac{\partial u_r}{\partial z}\right] \tag{3.8}$$

$$\tau_{\theta z} = \tau_{z\theta} = -\mu\left[\frac{\partial u_\theta}{\partial z} + \frac{1}{r}\frac{\partial u_z}{\partial \theta}\right] \tag{3.9}$$

Where,

$$\nabla.\vec{u} = \frac{1}{r}\frac{\partial}{\partial r}(ru_r) + \frac{1}{r}\frac{\partial u_\theta}{\partial \theta} + \frac{\partial u_z}{\partial z} \tag{3.10}$$

In addition to the Navier-Stokes equations, the general fluid continuity equation in cylindrical coordinates is written as the following:

$$\frac{\partial \rho}{\partial t} + \frac{1}{r}\frac{\partial}{\partial r}(\rho r u_r) + \frac{1}{r}\frac{\partial}{\partial \theta}(\rho u_\theta) + \frac{\partial}{\partial z}(\rho u_z) = 0 \tag{3.11}$$

The complete energy equation without any simplifying assumptions in cylindrical coordinates is given as follow:

$$\rho\, c_p \left[\frac{\partial T}{\partial t} + u_r \frac{\partial T}{\partial r} + \frac{u_\theta}{r}\frac{\partial T}{\partial \theta} + u_z \frac{\partial T}{\partial z}\right] = \rho\dot{q} + \frac{1}{r}\frac{\partial}{\partial r}\left(kr\frac{\partial T}{\partial r}\right) + \frac{1}{r}\frac{\partial}{\partial \theta}\left(\frac{k}{r}\frac{\partial T}{\partial \theta}\right) + \frac{\partial}{\partial z}\left(k\frac{\partial T}{\partial z}\right) + \beta T\left(\frac{\partial p}{\partial t} + u_r\frac{\partial p}{\partial r} + \frac{u_\theta}{r}\frac{\partial p}{\partial \theta} + u_z\frac{\partial p}{\partial z}\right) + \Phi \tag{3.12}$$

Where Φ the viscous dissipation rate is:

$$\Phi = 2\mu\left[\left(\frac{\partial u_r}{\partial t}\right)^2 + \left(\frac{1}{r}\frac{\partial u_\theta}{\partial \theta}\frac{u_r}{r}\right)^2 + \left(\frac{\partial u_z}{\partial z}\right)^2\right] + \mu\left[\left(\frac{1}{r}\frac{\partial u_r}{\partial \theta} + \frac{\partial u_\theta}{\partial r} - \frac{u_\theta}{r}\right)^2 + \left(\frac{\partial u_\theta}{\partial z} + \frac{1}{r}\frac{\partial u_z}{\partial \theta}\right)^2 + \left(\frac{\partial u_z}{\partial r} + \frac{\partial u_r}{\partial z}\right)^2\right] - \frac{2}{3}\mu\left(\frac{1}{r}\frac{\partial (ru_r)}{\partial r} + \frac{1}{r}\frac{\partial u_\theta}{\partial \theta} + \frac{\partial u_z}{\partial z}\right)^2 \tag{3.13}$$

The details on the derivation of these equations can be found in any standard compressible flow book (Anderson, 1982).

All previously mentioned equations do not include any simplifying assumptions. These equations describe the general behavior of a fluid motion inside a cylindrical container. In the following section, the simplified equations are obtained applying the axisymmetric assumption.

3.2. Axisymmetric Swirling Flow

According to the model geometry and flow conditions, the problem is considered axisymmetric. The axisymmetric assumption allows the modeling of the flow in two dimensions (2D). This assumption implies that there is no tangential gradients in the

flow. In other words, all the derivatives with respect to the tangential coordinates are zero ($\frac{\partial}{\partial\theta} = 0$). On the other hand, it must be noted that this assumption does not mean that tangential velocities are zero. Swirl velocities may or may not be zero ($u_\theta \neq 0$).
Based on this assumption the tangential momentum conservation equation for a 2D swirling flow is given as the following:

$$\frac{\partial}{\partial t}(\rho u_\theta) + \frac{1}{r}\frac{\partial}{\partial z}(r\rho u_z u_\theta) + \frac{1}{r}\frac{\partial}{\partial r}(r\rho u_r u_\theta) = \frac{1}{r}\frac{\partial}{\partial z}\left[r\mu\frac{\partial u_\theta}{\partial z}\right] + \frac{1}{r^2}\frac{\partial}{\partial r}\left[r^3\mu\frac{\partial}{\partial r}(\frac{u_\theta}{r})\right] - \rho\frac{u_r u_\theta}{r} \quad (3.14)$$

As seen in this equation all three components of velocity are appearing but only axial and radial spatial coordinates are present. This assumption ($\frac{\partial}{\partial\theta} = 0$) simplifies all the other governing equations as well.
Applying the axisymmetric assumption to the continuity equation 3.4 gives:

$$\frac{\partial\rho}{\partial t} + \frac{\partial}{\partial z}(\rho u_z) + \frac{\partial}{\partial r}(\rho u_r) + \frac{\rho u_r}{r} = 0 \quad (3.15)$$

The axial and radial momentum conservation equations respectively are found (Fluent, 2011):

$$\frac{\partial}{\partial t}(\rho u_z) + \frac{1}{r}\frac{\partial}{\partial z}(r\rho u_z u_z) + \frac{1}{r}\frac{\partial}{\partial r}(r\rho u_r u_z)$$
$$= -\frac{\partial p}{\partial z} + \frac{1}{r}\frac{\partial}{\partial z}\left[r\mu(2\frac{\partial u_z}{\partial z} - \frac{2}{3}(\frac{\partial u_z}{\partial z} + \frac{\partial u_r}{\partial r} + \frac{u_r}{r})\right] \quad (3.16)$$
$$+ \frac{1}{r}\frac{\partial}{\partial r}\left[r\mu\left(\frac{\partial u_z}{\partial r} + \frac{\partial u_r}{\partial z}\right)\right] + F_z$$

$$\frac{\partial}{\partial t}(\rho u_r) + \frac{1}{r}\frac{\partial}{\partial z}(r\rho u_z u_r) + \frac{1}{r}\frac{\partial}{\partial r}(r\rho u_r u_r)$$
$$= -\frac{\partial p}{\partial r} + \frac{1}{r}\frac{\partial}{\partial z}\left[r\mu\left(\frac{\partial u_r}{\partial z} + \frac{\partial u_z}{\partial r}\right)\right]$$
$$+ \frac{1}{r}\frac{\partial}{\partial r}\left[r\mu(2\frac{\partial u_r}{\partial r} - \frac{2}{3}(\frac{\partial u_z}{\partial z} + \frac{\partial u_r}{\partial r} + \frac{u_r}{r})\right] - 2\mu\frac{u_r}{r^2} \quad (3.17)$$
$$+ \frac{2}{3}\frac{\mu}{r}\left(\frac{\partial u_z}{\partial z} + \frac{\partial u_r}{\partial r} + \frac{u_r}{r}\right) + \rho\frac{u_\theta^2}{r} + F_r$$

Applying the axisymmetric assumption to 3.12 and neglecting the viscous dissipation rate provides the energy equation in the following simplified form:

$$\rho\, c_p \left[\frac{\partial T}{\partial t} + u_r\frac{\partial T}{\partial r} + u_z\frac{\partial T}{\partial z}\right] \quad (3.18)$$
$$= \rho\dot{q} + \frac{1}{r}\frac{\partial}{\partial r}\left(kr\frac{\partial T}{\partial r}\right) + \frac{\partial}{\partial z}\left(k\frac{\partial T}{\partial z}\right) + \beta T\left(\frac{\partial p}{\partial t} + u_r\frac{\partial p}{\partial r} + u_z\frac{\partial p}{\partial z}\right)$$

These equations are adapted in the 2D Axisymmetric Swirl solver in the commercial CFD software Ansys Fluent.

3.3. Turbulence Modeling

A simple definition of turbulence is the flow fluctuations in time and space. Turbulence is as an instability developing in laminar flow (Wilcox, 1998). High Reynolds number characterizes the turbulence as non-linear inertia terms interact with viscous terms. Various approaches can be used in order to include the effect of turbulence in the Navier-Stokes equations. For example, direct numerical simulation (DNS) can be used. However, currently DNS is not a practical approach due to the high cost of computations. Turbulence models are a practical method to predict turbulence with a reasonable cost. These models are mainly obtained by modifications in the unsteady Navier-Stokes equations involving fluctuating quantities and averages known as Reynolds Averaged Navier-Stokes (RANS) (Wilcox, 1998).

Swirling flow inside a pipe is highly turbulent. Thus, an accurate turbulence model should be introduced to capture the essence of relevant physics. In this section, two turbulence models that can more accurately predict turbulence in the flows involving swirls are introduced.

The first model is the RNG $k-\varepsilon$. This model belongs to the popular two equations $k-\varepsilon$ family of turbulence models, where k stands for turbulence kinetic energy and ε for turbulence dissipation rate. This model is obtained using a renormalization group (RNG) theory, which is a statistical technique, from the instantaneous Navier-Stokes equations. The transport equations for the RNG $k-\varepsilon$ model are given as follow:

$$\frac{\partial}{\partial t}(\rho k)+\frac{\partial}{\partial x_i}(\rho k u_i)=\frac{\partial}{\partial x_j}\left(\alpha_k \mu_{eff}\frac{\partial k}{\partial x_j}\right)+G_k+G_b-\rho\varepsilon-Y_M \qquad (3.19)$$

$$\frac{\partial}{\partial t}(\rho\varepsilon) + \frac{\partial}{\partial x_i}(\rho\varepsilon u_i) = \frac{\partial}{\partial x_j}\left(\alpha_\varepsilon \mu_{eff}\frac{\partial \varepsilon}{\partial x_j}\right) + C_{1\varepsilon}\frac{\varepsilon}{k}(G_k + C_{3\varepsilon}G_b) - C_{2\varepsilon}\rho\frac{\varepsilon^2}{k} - R_\varepsilon \qquad (3.20)$$

In these equations, α_k and α_ε represent the inverse effective Prandtl numbers for turbulence kinetic energy and its dissipation rate respectively. These numbers are calculated analytically based on the previously mentioned RNG theory. G_k and G_b stand for turbulence kinetic energy generation caused by the mean velocity gradients and buoyancy respectively. The effect of the fluctuating dilatation in compressible turbulence on the overall dissipation rate is represented through Y_M. For high Reynolds number the effective viscosity is given as $\mu_{eff} = \rho C_\mu k^2/\varepsilon$. The values for all the constants including $C_{1\varepsilon}$, $C_{1\varepsilon}$, $C_{1\varepsilon}$, and C_μ are given in Ansys Fluent user guide. For a swirl-dominated flow, Ansys Fluent modifies the turbulence viscosity as $\mu_t = \mu_{eff}\, f(\alpha_s, S, \frac{k}{\varepsilon})$, where S is the characteristic swirl number and α_s is a swirl constant that depends on the swirl intensity.

The parameter R_ε in the ε equation is the main difference between the RNG $k-\varepsilon$ model and the standard $k-\varepsilon$ model. This term is given by:

$$R_\varepsilon = \frac{\rho C_\mu \eta^3\left(1-\frac{\eta}{\eta_0}\right)}{1+\beta\eta^3}\frac{\varepsilon^2}{k} \qquad (3.21)$$

Here , η_0 , and β are constants obtained analytically. Because of R_ε term, the RNG $k-\varepsilon$ model reacts faster to the effects of rapid strain and streamline curvature.

The second suitable and highly accurate turbulence model for modeling swirling

flows is the Reynolds Stress Model (RSM). This highly elaborated model releases the isotropic eddy viscosity assumption in comparison to other models (ideal for anisotropic turbulence flow like swirling flows). The RSM closes RANS equations by solving Reynolds stresses transport equations, adding the equation 3.17 for the dissipation rate. The exact form of the Reynolds stresses are obtained by taking moments of the exact momentum equations. These exact equations include several unknown terms that require modeling assumptions. The complex transport equation for RSM model is given as follow:

$$\frac{\partial}{\partial t}\left(\rho\overline{u'_i u'_j}\right) + C_{ij} = D_{T,ij} + D_{L,ij} + P_{ij} + G_{ij} + \phi_{ij} + \varepsilon_{ij} + F_{ij} \tag{3.22}$$

Where,

$$C_{ij} = \frac{\partial}{\partial x_k}\left(\rho u_k \overline{u'_i u'_j}\right) \equiv Convection \tag{3.23}$$

$$D_{T,ij} = -\frac{\partial}{\partial x_k}\left[\rho\overline{u'_i u'_j u'_k} + \overline{p\left(\delta_{kj}u'_i + \delta_{ik}u'_j\right)}\right] \equiv Turbulence\ Diffusion \tag{3.24}$$

$$D_{L,ij} = \frac{\partial}{\partial x_k}\left[\mu\frac{\partial}{\partial x_k}(\overline{u'_i u'_j})\right] \equiv Molecular\ Diffusion \tag{3.25}$$

$$P_{ij} = -\rho\left(\overline{u'_i u'_k}\frac{\partial u_j}{\partial x_k} + \overline{u'_j u'_k}\frac{\partial u_i}{\partial x_k}\right) \equiv Stress\ Production \tag{3.26}$$

$$G_{ij} = -\rho\beta\left(g_i\overline{u'_j\theta} + g_j\overline{u'_i\theta}\right) \equiv Buoyancy\ Production \tag{3.27}$$

$$\phi_{ij} = \overline{p(\frac{\partial u'_i}{\partial x_j} + \frac{\partial u'_j}{\partial x_i})} \equiv Pressure\ Strain \tag{3.28}$$

$$\varepsilon_{ij} = 2\mu\overline{\frac{\partial u'_i}{\partial x_k}\frac{\partial u'_j}{\partial x_k}} \equiv Dissipation \tag{3.29}$$

$$F_{ij} = -2\rho\Omega_k\left(\overline{u'_j u'_m}\varepsilon_{ikm} + \overline{u'_i u'_m}\varepsilon_{jkm}\right) \equiv Production\ by\ System\ Rotation \tag{3.30}$$

In the RSM transport equation the terms in the equations of $D_{T,ij}$,G_{ij} ,ϕ_{ij}, and ε_{ij} require modeling assumptions (cannot be calculated directly). These modeling assumption are given in Ansys Fluent user guide. The rest of the terms are calculated directly. It is worth mentioning one of these models for the pressure-strain term useful in predicting swirling flows. Low-Re Stress-Omega model is a pressure-strain model based on the omega equations and Launder, Reece, and Rodi (LRR) model (Wilcox, 1998). In this model the wall reflections are excluded which makes this model ideal for flows over curved surfaces and flows involving swirls and vortices. This model have been used in this study for the cases solved with RSM turbulence model.

To conclude this section, it has been found that both of the RNG $k-\varepsilon$ and RSM models are appropriate in modeling the turbulence in the swirling flows. Each of these models has some advantages over the other. RNG $k-\varepsilon$ requires lesser computation cost (converges faster) and it is appropriate for flows including moderate swirl. On the other hand, RSM provides accurate prediction of the flows with high swirl intensity but the computation cost is higher due to the presence of extra equations. Pope (2000) in his book and Ansys Fluent user manual provide complete derivations and discussion of these turbulence models. Appendix B provides an example of turbulence models effect on the solution of a highly swirling flow.

3.4. CFD Software Set-Up

The purpose of this section is to describe the computation set-up. The commercial CFD solver Ansys Fluent has been used in order to obtain the solution of the swirling flow inside the cylindrical chamber.

The general setup is a steady state pressure-based solver with an absolute velocity

formulation. For the 2D cases, the Axisymmetric Swirl option has been activated. Fluids such as air and water with modified properties based on the information provided in the problem statement chapter have been used. The solution method is viscous flow with an appropriate turbulence model. As mentioned in previous section the $k-\varepsilon$ RNG Swirl Dominated Flow with Standard Wall Functions and the Stress-Omega, Reynolds Stress Model with Low-Re and Shear Flow corrections are two suitable turbulence models.

The swirling flow is obtained by a velocity-inlet boundary condition instead of using a swirl generator. The following boundary conditions are applied to both 2D and 3D models.

- **Inlet :** velocity-Inlet (velocity component specification $u_\theta \; and \; u_z$)
- **Wall :** stationary wall with no slip condition
- **Outlet :** pressure-outlet
- **Axis of symmetry:** axis (only 2D models)

The pressure discretization is another important factor in modeling of swirling flows. The PRESTO! (PREssure Staggering Option) scheme has been used. Discrete continuity balance is used in this scheme and it is available for all type of meshes. The PRESTO! scheme is strongly recommended for flows with high swirl intensity and strongly curved domains (Fluent, 2006).

In order to obtain a faster convergence in the flows involving swirls, it is appropriate to start the calculation in absence of swirl (just axial flow). This will provide an initial guess for the solver. The swirl with low intensity can be introduced in the next step. This process can be continued with gradually increasing the swirl intensity to the desired intensity. This concludes the software settings section.

4. Results Analysis

The following fluid models and software set-ups have been utilized: 2D incompressible gas, 2D incompressible liquid, 3D incompressible gas, and 2D compressible gas. A discussion on each of these models is provided in the following sections.

4.1. 2D Incompressible Gas

The first and simplest case to be analyzed is the 2D incompressible case. A simple structured mesh is generated using Pointwise (CFD mesh generator software). Figure 4.1 represents the axisymmetric structured mesh where the radius of the cylinder is $r = 0.05\ m$ and the length is taken as $l = 1.4\ m$ based on the dimensions provided in Chapter 2. Figure 4.2 shows the near wall treatment where the mesh is finer to include the boundary layer prediction.

Figure 4.1 2D axisymmetric structured mesh generated in Pointwise.

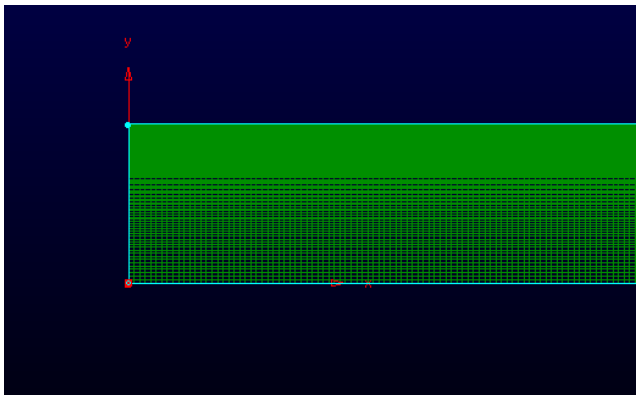

Figure 4.2 Zoom in to the left end of the mesh shown in Figure 4.1.

In order to obtain a mesh independent analysis, two versions of 2D structured mesh are generated. A coarse mesh including $\sim 80K\ cells$ and a fine version including $\sim 240K\ cells$. The maximum cell aspect ratio for both versions is ~ 7. In order to obtain consistent results, the same meshes for all the other 2D cases have been utilized.

After extracting the meshes from Pointwise and loading them in the Ansys Fluent the specific software set up given in section 3.4 is implemented. The operation conditions are based on the data provided in chapter 2. The Inlet velocity boundary condition as a combination of the tangential and axial velocity components satisfies Reynolds number of $\approx 5 \times 10^5$.

After considering various scenarios for inlet boundary condition and different turbulence models, significant results are obtained. In the following sections, some of these interesting results are presented.

4.1.1. 2D Incompressible Gas with RNG $k-\varepsilon$ Turbulence Model

In this section the results obtained from a 2D incompressible gas case using the RNG $k-\varepsilon$ turbulence model are presented. The velocity profiles describing the flow behavior across the whole model are obtained. Figure 4.3 shows the tangential (swirl) velocity at a

location ($^{x}/_{l} = 0.4$) in the model as a function of the cylinder radius r . As it is expected the tangential velocity at the core is zero and reaches a maximum value near the wall and goes back to zero at the wall. It has been observed that this maximum value in some cases appears at a location close to the center. This observation is shown in the counter plots presented in the rest of this section.

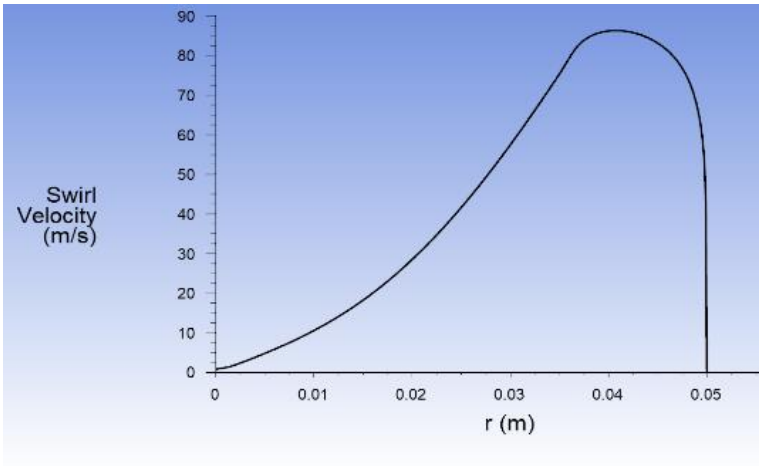

Figure 4.3 Tangential velocity at $^{x}/_{l} = 0.4$ (2D incompressible RNG k-ε).

In Figure 4.4, the axial velocity profile is presented. Like the tangential velocity, the axial velocity riches a maximum near the wall and goes to zero at the wall as expected.

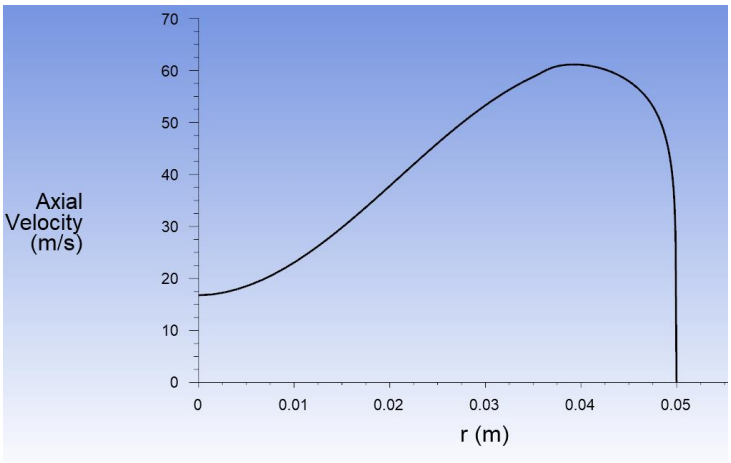

Figure 4.4 Axial velocity at $x/l = 0.4$ (2D incompressible RNG k-ε).

The last velocity profile is that of the radial velocity shown in Figure 4.5. The radial velocity values are small compared to axial and tangential velocity. This is due to the boundary conditions implemented ($u_r = 0$).

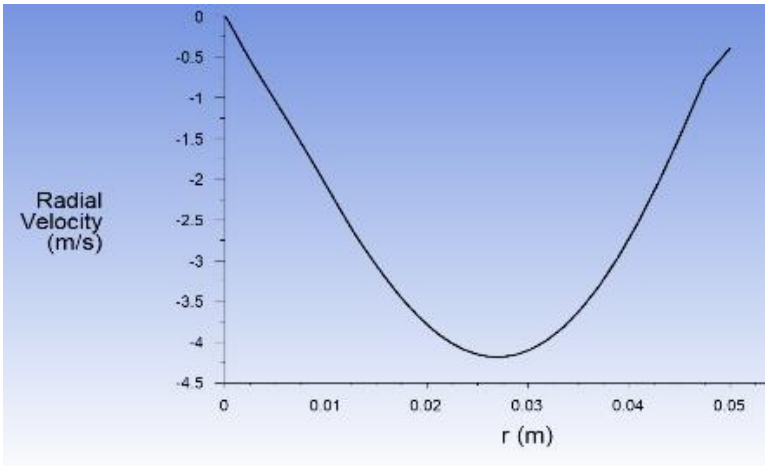

Figure 4.5 Radial velocity at $x/l = 0.4$ (2D incompressible RNG k-ε).

Based on the velocity-inlet boundary condition applied and the ratio of the tangential velocity over axial velocity ($\frac{u_\theta}{u_z}$) an unstable behavior of the flow has been observed.

This behavior is classified based on a critical value of $\frac{u_\theta}{u_z} = 2.5$. This ratio is confirmed by all the other cases and scenarios analyzed in this study. In order to provide a better understanding of these observations the tangential velocity contour plots are presented in Figures 4.6-8. For all the scenarios in which $\frac{u_\theta}{u_z} \lesssim 2.5$, approximately a stable behavior has been predicted. A core region in which the velocity tends to be zero have been identified (Figure 4.6). The diameter of this region is approximately 10% of the whole diameter.

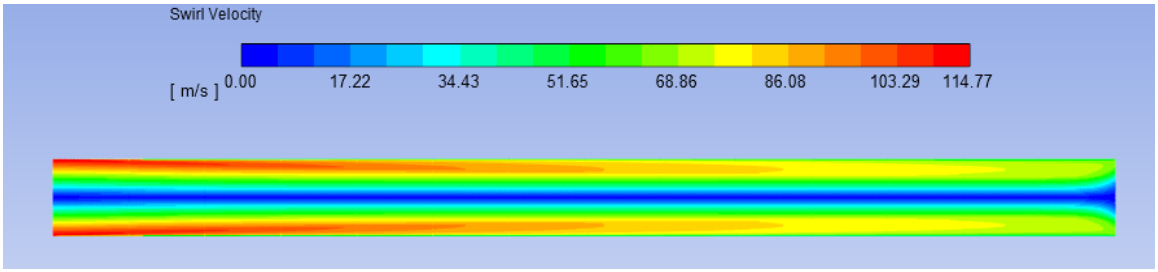

Figure 4.6 Tangential velocity contour with a velocity-inlet of $\frac{u_\theta}{u_z} \lesssim 2.5$.

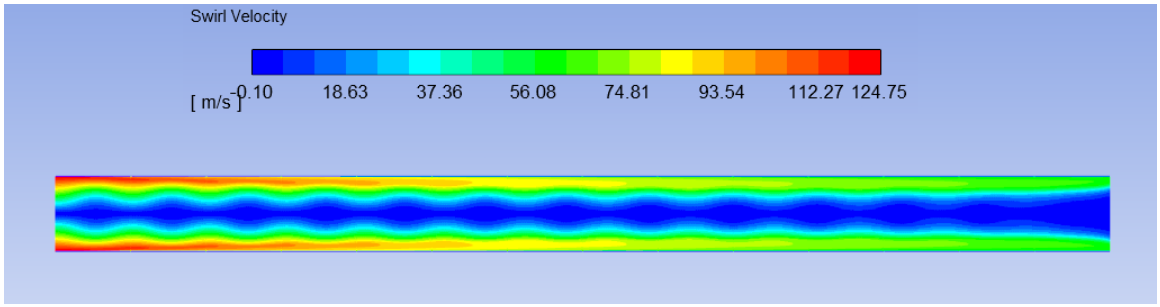

Figure 4.7 Tangential velocity contour with a velocity-inlet of $\frac{u_\theta}{u_z} \approx 2.5$.

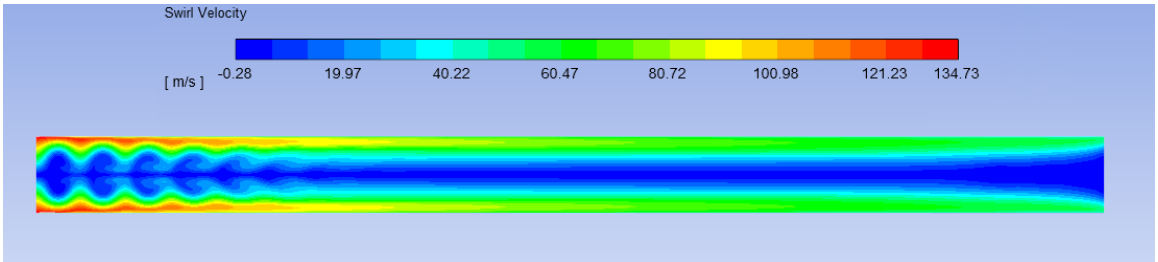

Figure 4.8 Tangential velocity contour with a velocity-inlet of $\frac{u_\theta}{u_z} \gtrsim 2.5$.

By increasing the velocity ratios and reaching the limiting case of $\frac{u_\theta}{u_z} \approx 2.5$, a periodic wavy behavior of swirl velocity has been observed (Figure 4.7). The core diameter in this case varies approximately from 10% up to 20% of the whole diameter. By further increasing the $\frac{u_\theta}{u_z}$ ratio, a different unstable pattern has been observed (Figure 4.8). An intense vortex behavior at the inlet appears which soon decays and the flow becomes stable. Another important observation in all of the contour plots is that the swirl intensity decays as the flow approaches the downstream outlet. A detail discussion on swirl decay is provided in section 4.4.

In order to understand the secondary flow field observed in Figure 4.8, the velocity vectors have been plotted. Figure 4.9 represents the 2D velocity vector field (u_z andu_r). This plot displays the counter-rotating axisymmetric toroidal vortices. The observed vortices are similar to the Taylor vortices in the classic Taylor-Couette flow in the gap between two concentric rotating cylinders. This similarity is furfure discussed in the following sections.

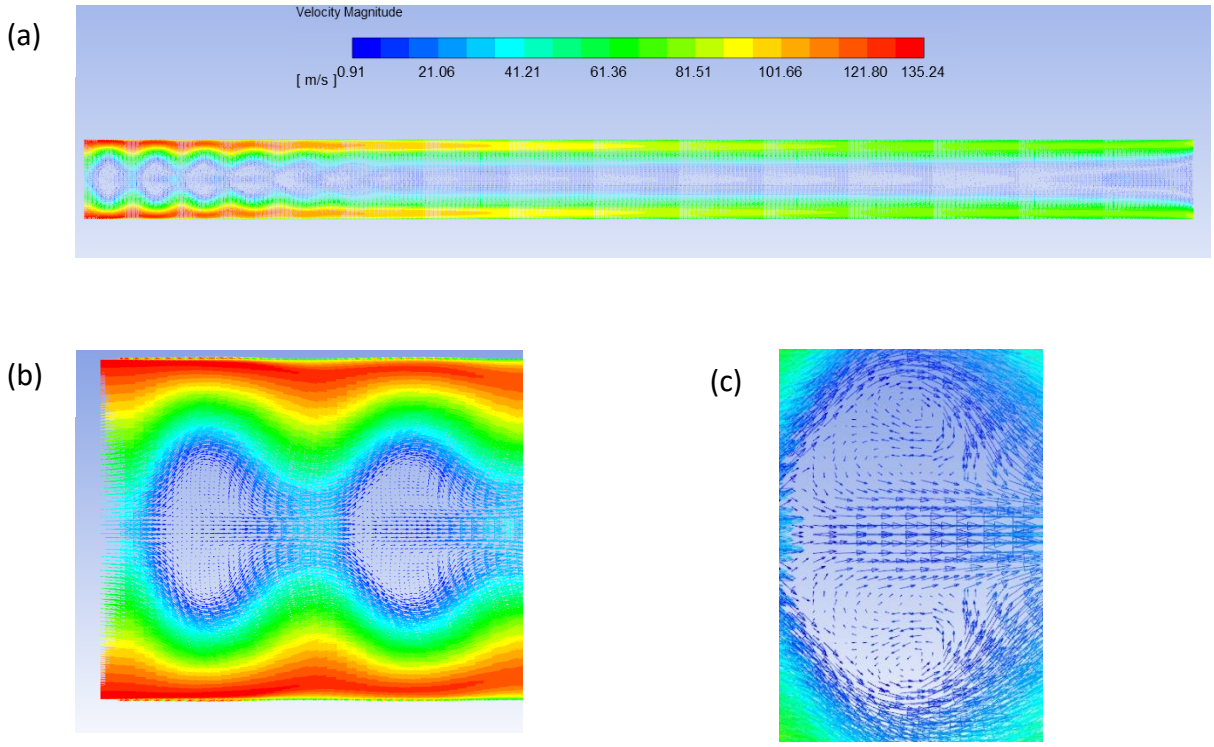

Figure 4.9 (a) Velocity vectors (u_z *and* u_r)) colored by bulk velocity magnitude representing counter-rotating axisymmetric toroidal vortices. (b) Zoom in on the left-end and (c) further zoom on vortices.

4.1.2. 2D Incompressible Gas with RSM Turbulence Model

This section presents the results obtained for the same 2D incompressible gas case presented in the previous section but with a stress-omega Reynolds stress turbulence model. The tangential velocity and axial velocity profiles are presented in Figure 4.10 and Figure 4.11 respectively. The radial velocity component is negligible in comparison to other velocity components.

The curves are in a good agreement with those found with RNG k-ε model. However, the RSM predicts the maximum values differently. This is due to the different near-wall treatment approach in this model. As it is described in turbulence modeling section (3.3), RSM resolves the high intensity swirling flows more accurately than the other models.

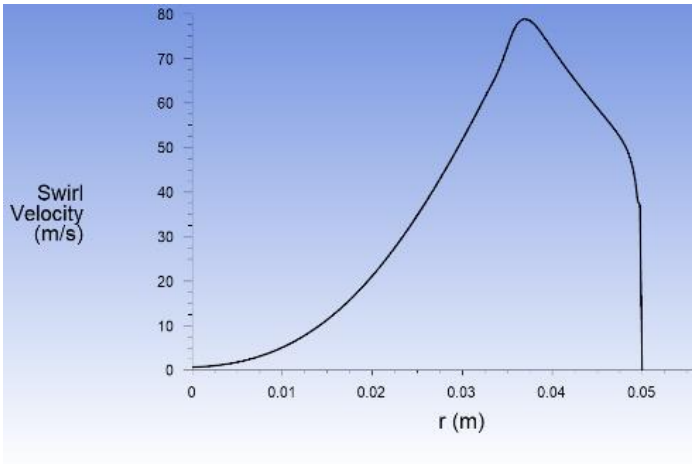

Figure 4.10 Tangential velocity at $x/l = 0.4$ (2D incompressible RSM).

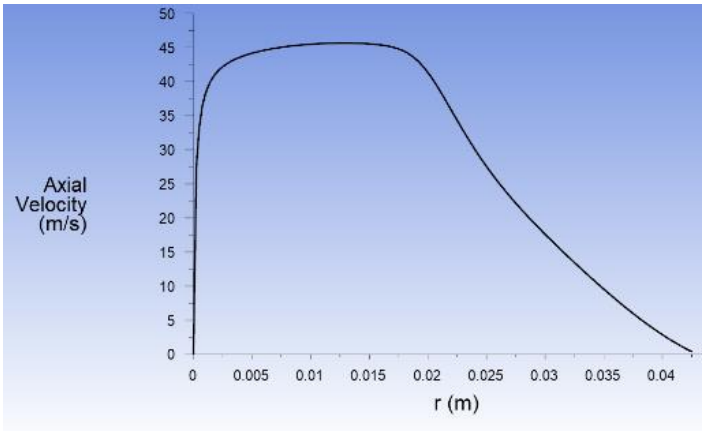

Figure 4.11 Axial velocity at x/l = 0.4 (2D incompressible RSM).

The tangential velocity counter plots obtained with RSM model are similar to the previously presented plots although minor differences have been observed. To conclude this section the Taylor-like vortices obtained with this turbulence model are presented in Figure 4.12.

(a)

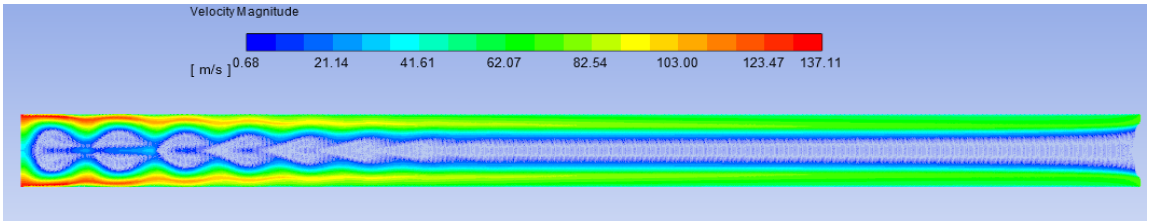

(b)

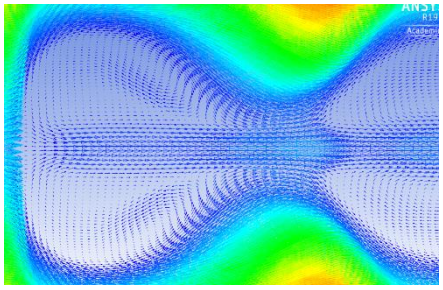

(c)

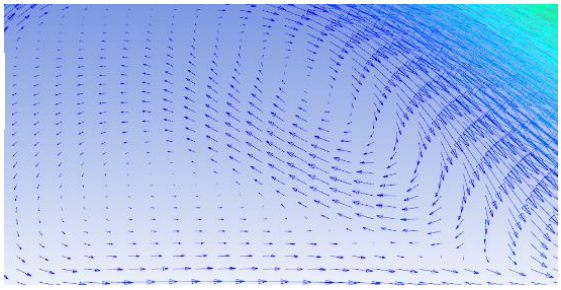

Figure 4.12 (a) Velocity vectors (u_z *and* u_r) colored by bulk velocity magnitude representing counter-rotating axisymmetric toroidal vortices (2D incompressible RSM). (b) Zoom in on the left-end and (c) further zoom on vortices.

4.2. 2D Incompressible Liquid

In order to validate the physical meaning of the results obtained with an incompressible gas assumption, a case using water as the fluid have been analyzed. In contrast to the previous case where the gas mixture is assumed incompressible, water as a purely incompressible fluid is chosen. This is to omit the effects of negligence of the compressible behavior of the gas on the solutions. In order to achieve comparable results with previously obtained solutions, the target Reynolds number ($\approx 5 \times 10^5$) is implemented in the velocity-inlet boundary condition. The velocity profiles are presented in Figure 4.13-15. These results are obtained using a RNG k-ε turbulence model. As it is shown in the figures, the velocity profiles are in agreement with the 2D gas cases.

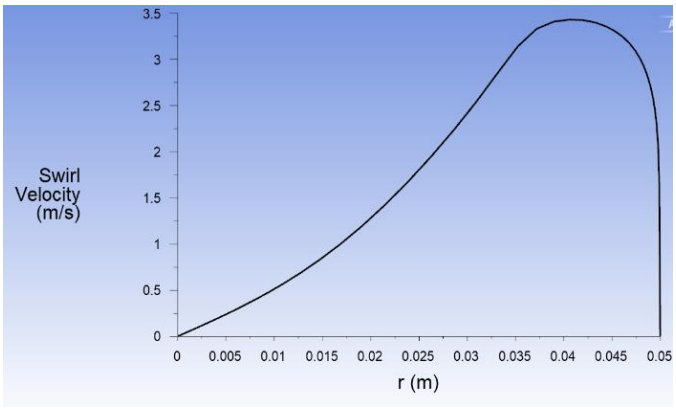

Figure 4.13 Tangential velocity at $^{x}/_{l} = 0.4$ (2D Water).

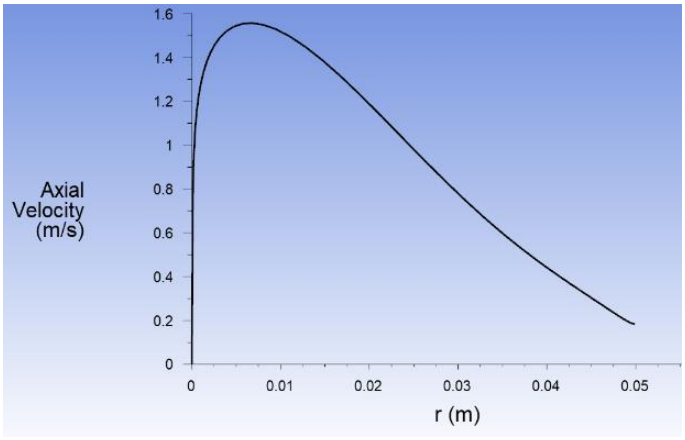

Figure 4.14 Axial velocity at $^{x}/_{l} = 0.4$ (2D Water).

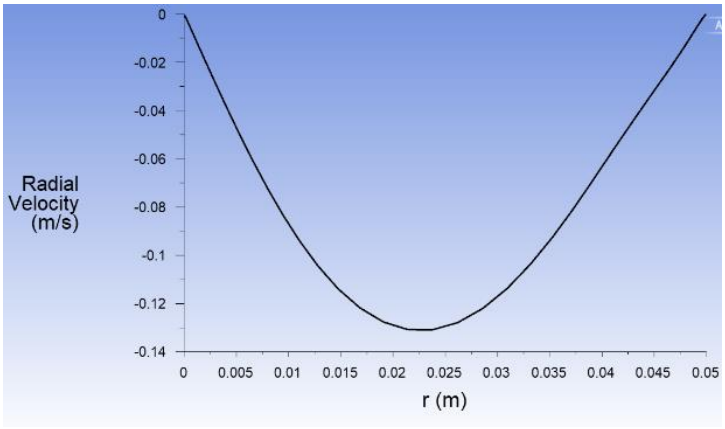

Figure 4.15 Radial velocity at $x/l = 0.4$ (2D Water).

4.3. 3D Incompressible Gas

In order to validate the results obtained in 2D cases, a sample 3D model has been analyzed. In the 3D geometry the same dimensions as the 2D model has been used in order to obtain comparable results. Figure 4.16 shows the structured axisymmetric 3D mesh created in Pointwise. In generation of this mesh a butterfly topology has been used to avoid the pole (singularity) in the front and aft-end of the cylinder.

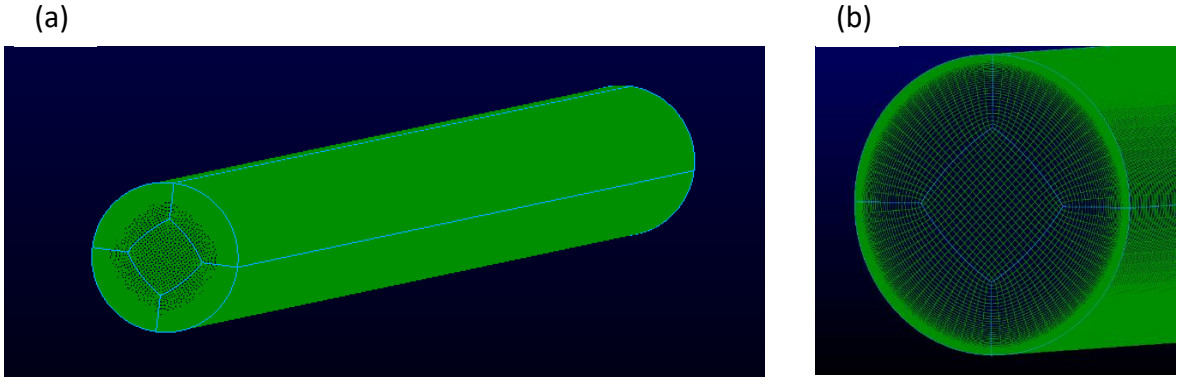

Figure 4.16 (a) The 3D structured axisymmetric grid generated in Pointwise and (b) zoom in view to one side of the cylinder.

The same conditions and software set up applied to the 2D incompressible gas case using

the RNG $k-\varepsilon$ model have been applied to the 3D model. In the remaining parts of this section, some of relevant results are presented.

Figure 4.17 shows an isometric view of the velocity streamlines generated using Tecplot. In this figure, the spiral flow pattern caused by combination of the tangential and axial velocities is clearly observed.

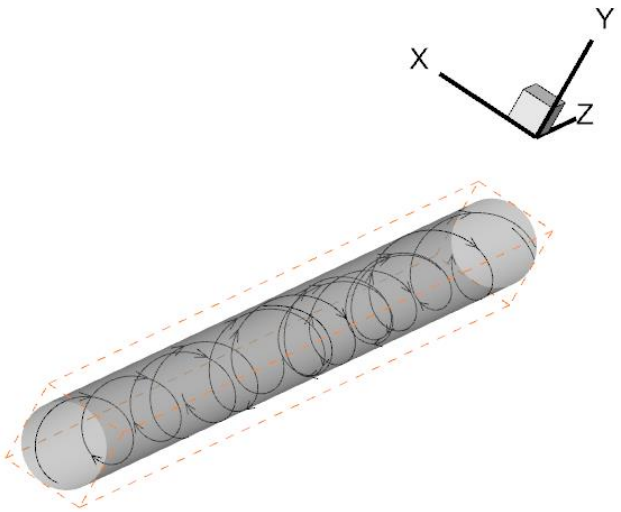

Figure 4.17 Velocity streamlines in the 3D case (Tecplot).

In order to compare the 3D results with those in 2D cases, the results obtained at the critical case where $\frac{u_\theta}{u_z} \approx 2.5$ are presented here. Figure 4.18 represents the tangential velocity contour plot over a vertical cross-section of the cylinder. This plot is similar to the previously presented results in Figure 4.7.

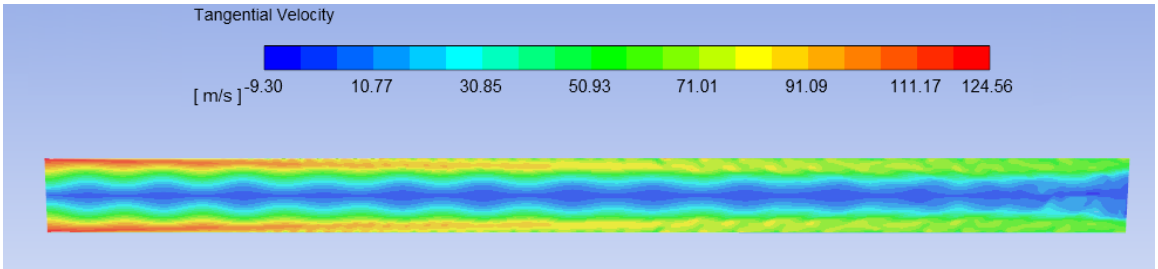

Figure 4.18 Tangential velocity contour over a vertical cross-section of the 3D model.

All the other results obtained with the 3D model are also in good agreement with the 2D results. Figures 4.19-21 provide each velocity component contour plot over a horizontal cross-section of the 3D. These profiles are obtained at the critical condition of $\frac{u_\theta}{u_z} \approx 2.5$ at a location of $x/l = 0.4$.

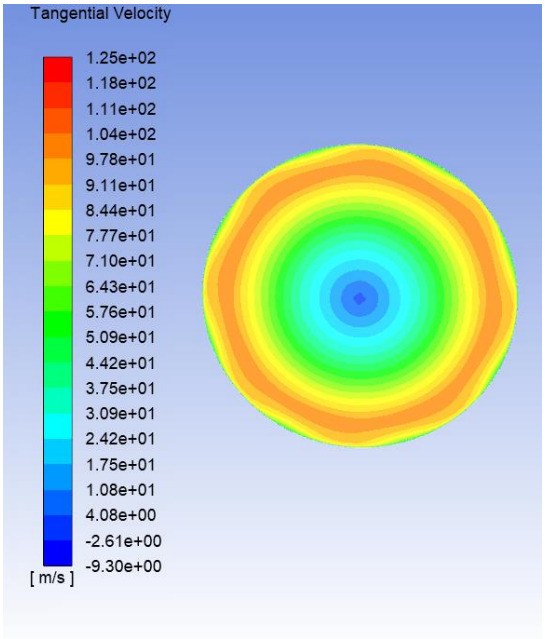

Figure 4.19 Tangential velocity contour over a horizontal cross-section at $x/l = 0.4$ (3D case).

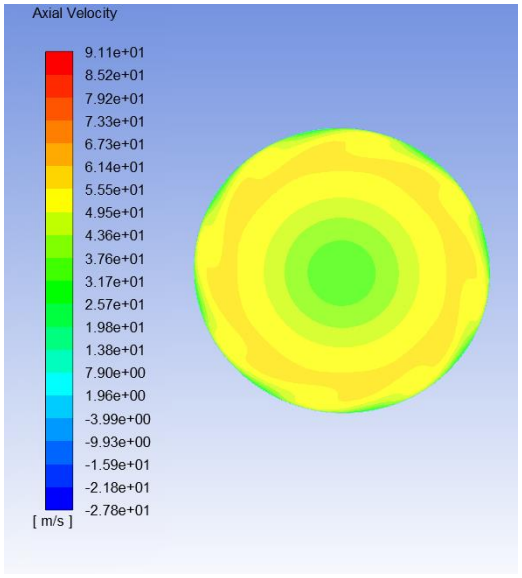

Figure 4.20 Axial velocity contour over a horizontal cross-section at $^{x}/_{l} = 0.4$ (3D case).

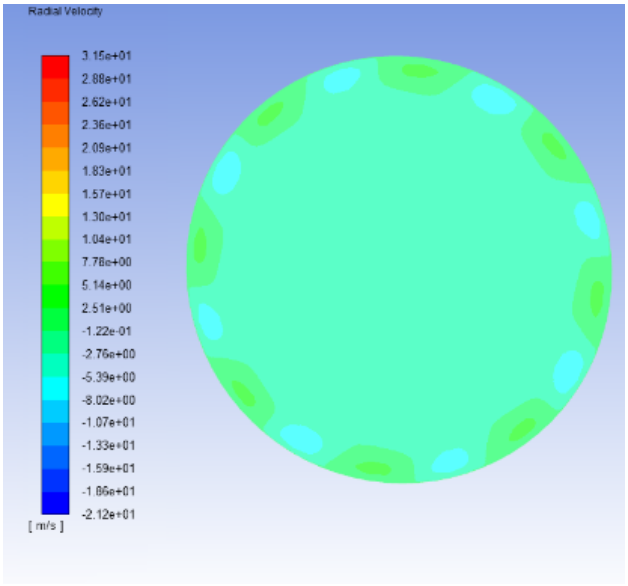

Figure 4.21 Radial velocity contour over a horizontal cross-section at $^{x}/_{l} = 0.4$ (3D case).

4.4. 2D Compressible Gas

The purpose of this section is to present the velocity profiles obtained from a case in which the flow is compressible. Although based on the data provided in chapter 2 the flow under examination can be assumed incompressible, a CFD software set-up solving the compressible flow has been carried out. For this case, a density-based solver using the ideal gas law for the density calculation has been implemented. In the following figures, the velocity profiles are presented.

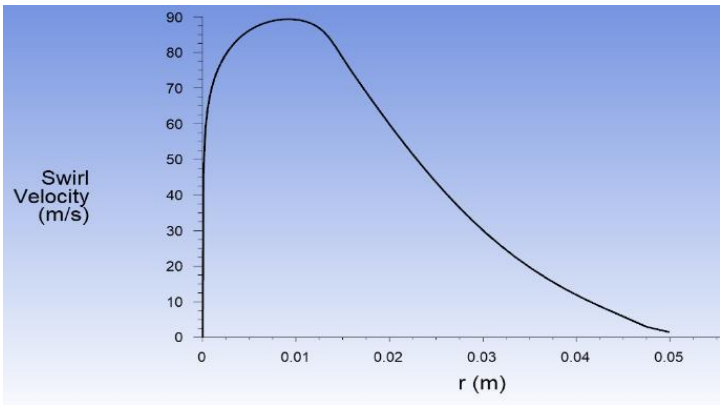

Figure 4.22 Tangential velocity at $x/l = 0.4$ (2D compressible case).

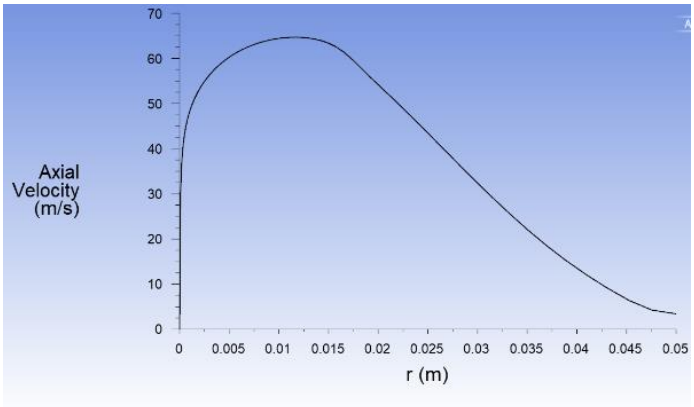

Figure 4.23 Axial velocity at $x/l = 0.4$ (2D compressible case).

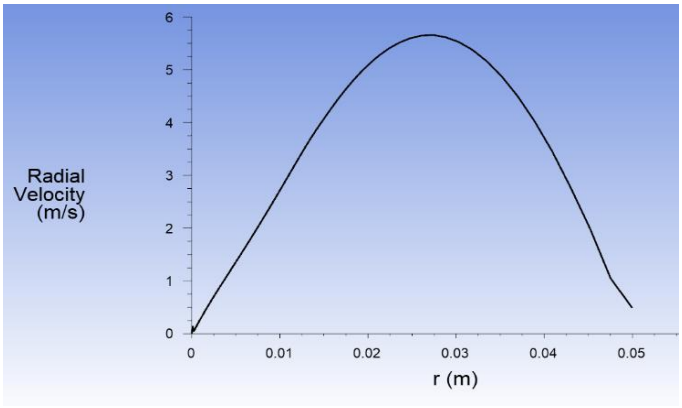

Figure 4.24 Radial velocity at $x/l = 0.4$ (2D compressible case).

5. Discussion of Findings

In this chapter, a detailed analysis of the previously presented results is provided. First a discussion of the swirl intensity decay is given. Second, the main observation of the results, which is the presence of the Taylor-Like vortices at certain critical conditions, is discussed.

5.1. Swirl Number and Swirl Decay

Swirling flows are a combination of the axial and tangential motion of the fluid in a helical path. Swirl number S is a standard non-dimensional number representing swirl intensity. Based on Gupta, Lilley, and Syred (1984) swirl number defines as the ratio of the angular momentum flux and the axial momentum flux of the fluid.

$$S = \frac{G_\theta}{G_x R} \tag{5.1}$$

Here R is the hydraulic radius of the pipe.

Based on angular and axial momentum flux the equation 5.1 can be written as:

$$S = \frac{\int_0^R (\rho u_x u_\theta + \rho \overline{u_x" u_\theta"}) r^2 dr}{R \int_0^R (\rho u_x^2 + \rho \overline{u_x'^2} + (p - p_\infty)) r dr} \tag{5.2}$$

Rocklage-Marliani, Schmidts, and Ram (2003) later give a simplified version of this equation:

$$S = \frac{\int_0^R u_x u_\theta r^2 dr}{R \int_0^R u_x^2 r dr} \tag{5.3}$$

All the variables presented in equation 5.3 are extracted from the CFD software Ansys Fluent. These data are then uploaded in Matlab. By Trapezoidal numerical integration of the equation 5.3 Swirl number S values are calculated at different locations of the cylinder. S values are ranging from 0.45 to 1.24. These results are shown in Figure 5.1. These Results are in a good agreement with the experimental and numerical results found in the literature (Von Lavante & Yao, 2012).

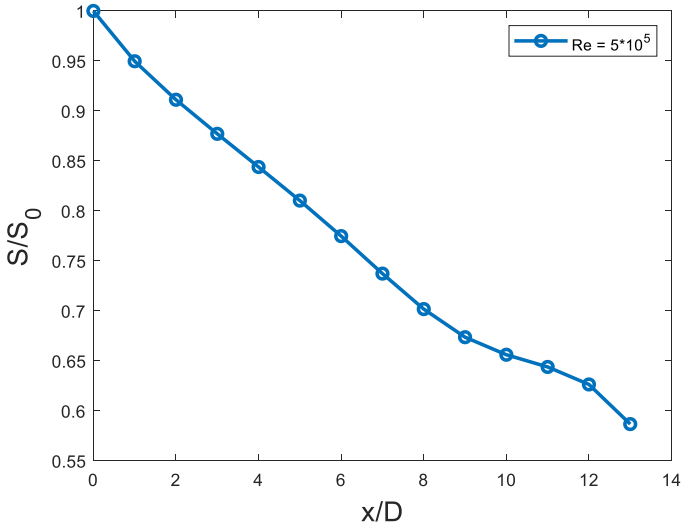

Figure 5.1 Relative Swirl number decay as a function of x/D.

Due to the adverse pressure gradients and vortex breakdowns swirl components decay as approaching downstream. Parchen and Steenbergen (1998) demonstrate this

exponential decay.

$$S = S_0 e^{-\beta x/D} \tag{5.4}$$

In this relation, S_0 is the initial swirl number at the inlet and β represents the decay rate. The importance of the initial conditions are clear from this equation. It has been also shown that the rate of decay is a function of Reynolds number. Figure 5.2 represents the relative swirl number decay for different Reynolds numbers.

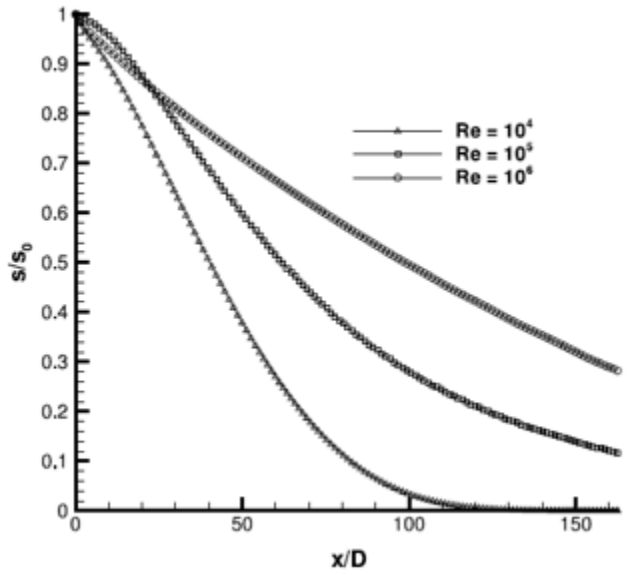

Figure 5.2 Relative Swirl number decay as a function of x/D for a range of Reynolds numbers (Von Lavante & Yao, 2012).

In Figure 5.3, the relative swirl number decay for different cases is presented. Here, the plots for incompressible gas case using two different turbulence models and the case with water are presented. The Reynolds number for these cases is equal to 5×10^5. After

comparing these plots with the literature, the RSM turbulence model is in a better agreement.

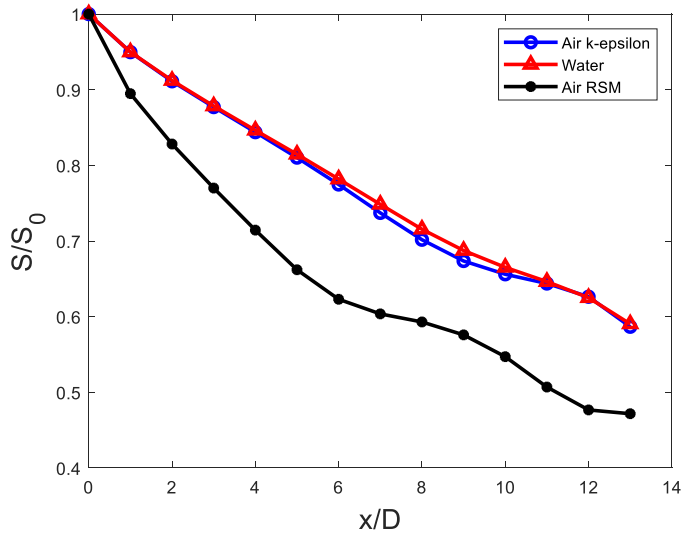

Figure 5.3 Relative Swirl number decay as a function of x/D (2D cases).

5.2. Taylor-Like Vortices

The results analysis ilustrates the existence and generation of the vortices in the flow field. After reviewing literature on the family of the rotating flows, similar results are identified in the classic Taylor-Couette flow and the free-surface vortex flows. A brief description and similarities to the obtained results in this study of each of these flow systems are presented in this section.

5.2.1. Taylor-Couette Flow

The classic Taylor-Couette flow refers to the rotating of an incompressible viscous flow in the gap between two coaxial rotating cylinders (with radii R_1 & R_2 and angular velocities of $\Omega_1 \& \Omega_2$ (Figure 5.3)).

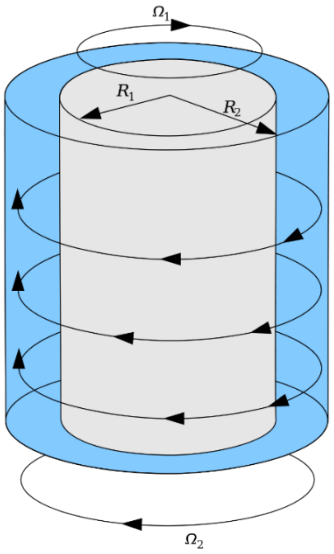

Figure 5.4 Taylor-Couette flow system.

The exact steady solution of Taylor-Couette flow system are obtained from the equations 3.1-3(Navier-stokes) and 3.10 (continuity) in the following form:

$$u_r = u_z = 0, \quad u_\theta = V(r) = Ar + \frac{B}{r} \tag{5.5}$$

Where A and B are two arbitrary constants determined by the boundary conditions of the system.

In order to investigate the stability of the Taylor-Couette flow system, the perturbation (disturbance) equations are developed. For example, a general disturbance on the basic solution given in 5.5 is superimposed as follow:

$$u_\theta = V(r) + v'(r, \theta, z, t) \tag{5.6}$$

Substituting these disturbances in equations 3.1-3 and 3.10, a system of four non-linear partial differential equations is obtained (these equations and a detailed discussion on instability analysis are found in the books by Chandrasekhar (1961) and Koschmieder (1993)). These equations are linearized assuming perturbations are axisymmetric (more details in section 3.2). The nondimensionalization of these linear equations leads to a very important non-dimensional parameter called Taylor number given as:

$$T = \frac{R_1 \Omega_1^2 (R_2 - R_1)^3}{\nu^2} \tag{5.7}$$

Taylor number has the same physical meaning of Reynolds number. Both of these numbers are a ratio of the inertial forces over viscous forces. Taylor number is the non-dimensional control parameter for the Taylor-Couette flow system. This system is unstable for the Taylor numbers greater than a critical value T_c (depends on Ω). For T slightly greater than T_c, this instability leads to generation of toroidal vortices spaced regularly in the axial direction (Figure 5.4). By further increasing T a secondary instability develops that causes a wavy vortex motion.

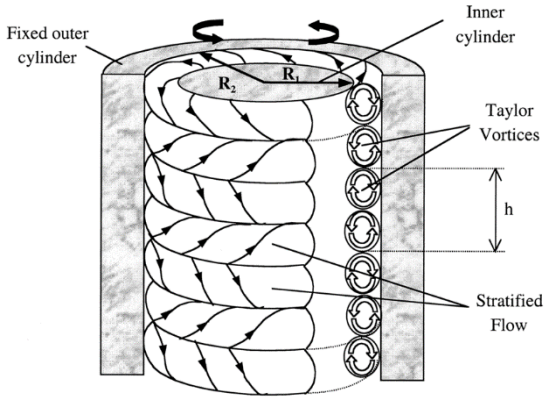

Figure 5.5 Taylor vortices visualization (Moser et al., 2002).

The critical Taylor number for laminar flow is $T_c = 1708$, but this number for turbulent flow is different. At $T \approx 1.6 \times 10^5$ the flow can be considered turbulent. Smith & Townsend (1982) experimental work over a wide range of Taylor numbers find the critical number to be approximately $T_c \approx 5.8 \times 10^8$. The Taylor number for the critical 2D incompressible case ($\frac{u_\theta}{u_z} \approx 2.5$) has been calculated as $T_c' \approx 1.6 \times 10^8$ which is consistent with the experimental results.

5.2.2. Free-surface vortex flow

In general, free-surface vortices are the result of natural or artificial strong field circulation ($\Gamma = u_\theta 2\pi r$). This phenomenon is characterized by turbulence through the vortex Reynolds number $\mathrm{Re}_\Gamma = \Gamma/\nu$. Similar to Taylor-Couette flow the instabilities in free-surface vortex system result in generation of Taylor-like vortices. Mulligan shows that the air core in this flow system acts like the rotating inner cylinder in Taylor-Couette system (Figure 5.5). In order to be consistent with Taylor-Couette flow system Mulligan formulated a dimensionless driving control parameter given as:

$$M = \frac{v_a^2}{r_a}\frac{(r_o - r_a)^3}{\nu^2} \tag{5.8}$$

Where r_a represents the radius of the air core and the r_o is the outer boundary and v_a is the tangential velocity of the air core characterized by circulation ($v_a = \Gamma/r_a$). This number (M) is exactly Taylor number adapted for free-surface vortex flow system.

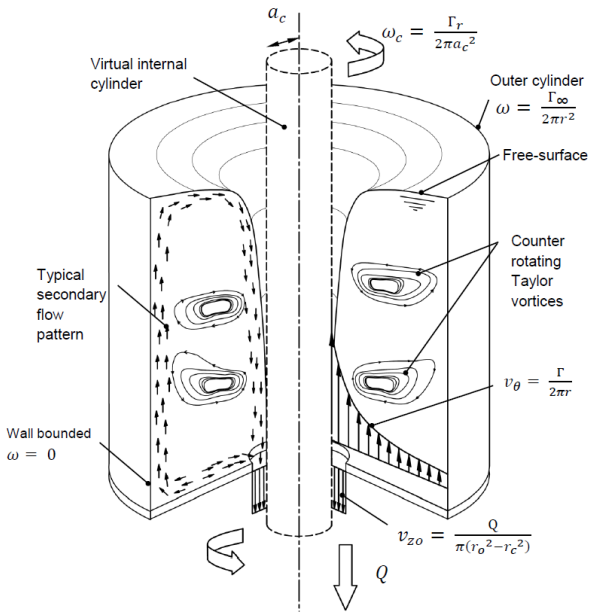

Figure 5.6 Free-surface vortex flow system with full virtual air core (Mulligan, 2015).

Taylor-like vortices are observed in Mulligan's study at a Reynolds number of approximately $\mathrm{Re}_\Gamma = 1.7 \times 10^5$ and $M = 6.4 \times 10^5$. Considering the critical 2D incompressible case ($\frac{u_\theta}{u_z} \approx 2.5$) these numbers are estimated as $\mathrm{Re}_\Gamma{}' = 3.5 \times 10^5$ and $M' = 4 \times 10^5$. It should be noted that this is just a crude approximation and is brought here for comparison purposes.

6. Summary and Conclusion

In this thesis the swirling flow behavior in the context of hybrid rocket engines has been studied. The operation conditions of this type of rocket is used as the main structure of the problem formulation. Computational fluid dynamics (CFD) has been chosen as the main methodology of approaching this problem. The axisymmetric swirling flow inside a cylindrical chamber with the RNG k-ε and the RSM turbulence models has been modeled in Ansys Fluent CFD solver. In order to ensure the physical meanings of the results various 2D and 3D models involving different boundary conditions have been examined.

After running and analyzing various cases, it is found that defining the inlet boundary condition with a tangential to axial velocity ratio of $\frac{u_\theta}{u_z} \approx 2.5$ is a critical condition. This critical value results in formation of a secondary flow field composed of wavy toroidal vortices spaced regularly in axial direction. The core diameter of the axisymmetric swirl flow inside a cylinder in presence of these instabilities is estimated 10-20% of the cylinder diameter. In order to verify the work done on this study, future experimental studies are required.

The results obtained in this study provide a basic insight to the behavior of turbulent swirling flow inside a cylindrical container. In order to improve this study for a hybrid rocket application, further considerations are required. The future study of this topic could potentially involve the heat addition (or combustion) to the flow.

REFERENCES

Arena, Z., Athougies, A., Rodulfo, A., & DeTurris, D. (2011). *Swirl Injection Hybrid Rocket Motor Design and Testing*. In 47th AIAA/ASME/SAE/ASEE Joint Propulsion Conference & Exhibit (p. 5676)

Bellomo, N., Barato, F., Faenza, M., Lazzarin, M., Bettella, A., & Pavarin, D. (2011, August). *Numerical and experimental investigation on vortex injection in hybrid rocket motors*. In 47th AIAA/ASME/SAE/ASEE Joint Propulsion Conference & Exhibit (p. 5675).

Chandrasekhar, S. (2013). *Hydrodynamic and hydromagnetic stability*. Courier Corporation.

Chiaverini, M., & Kuo, K. (2007). *Fundaments of hybrid rocket combustion and propulsion (Vol. 218)*. Reston, Virginia: American Institute of Aeronautics and Astronautics.

Davey, A., Di Prima, R. C., & Stuart, J. T. (1968). *On the instability of Taylor vortices*. Journal of Fluid Mechanics, 31(1), 17-52.

Fluent, A. N. S. Y. S. (2011). *Ansys fluent theory guide*. ANSYS Inc., USA, 15317, 724-746.

Gupta, A. K., Lilley, D. G., & Syred, N. (1984). *Swirl Flows*. Tunbridge Wells, England: Abacus Press.

Halpenny, E., & Majdalani, J. (2008). *The Bidirectional Vortex with Sidewall Injection*. In 44th AIAA/ASME/SAE/ASEE Joint Propulsion Conference & Exhibit (p. 5018).

Jeevahan, J., Chandrasekaran, M., Mageshwaran, G., & Joseph, G. B. (2016). *Analysis of the effect of geometry of vortex tube on cold side and hot side air stream temperatures*. Journal of Chemical and Pharmaceutical Sciences, 9(3), 2474-2477.

Jones, C., Myre, D., & Cowart, J. (2009). *Performance and analysis of vortex oxidizer injection in a hybrid rocket motor*. In 45th AIAA/ASME/SAE/ASEE Joint Propulsion Conference & Exhibit (p. 4938).

Koschmieder, E. L. (1993). *Bénard cells and Taylor vortices*. Cambridge University Press.

Lee, T. S., & Potapkin, A. (2002). *The performance of a hybrid rocket with swirling GOx injection*. NATIONAL CHENG KUNG UNIV TAINAN (TAIWAN).

Majdalani, J., & Vyas, A. (2004). *Rotational axisymmetric mean flow for the vortex injection hybrid rocket engine*. In 40th AIAA/ASME/SAE/ASEE Joint Propulsion Conference and Exhibit (p. 3475).

Marquardt, T. A., Majdalani, J., & Cecil, O. M. (2015). *On the Quadrupole Vortex Motion in a Right-Cylindrical Hybrid Rocket Engine*. In 51st AIAA/SAE/ASEE Joint Propulsion Conference (p. 3743).

Motoe, M., & Shimada, T. (2009). *Head-end injected swirling gas flow in a chamber*. In 45th AIAA/ASME/SAE/ASEE Joint Propulsion Conference & Exhibit (p. 5025).

Mulligan, S. (2015). *Experimental and numerical analysis of three-dimensional free-surface turbulent vortex flows with strong circulation*. PhD dissertation.

Myre, D., Caton, P., Cowart, J., & Jones, C. (2010). *Exhaust gas analysis of a vortex oxidizer injection hybrid rocket motor*. In 46th AIAA/ASME/SAE/ASEE Joint Propulsion Conference & Exhibit (p. 6548).

Ohyama, S., Aso, S., Hirata, Y., Araki, K., Ohe, K., Tani, Y., & Shimada, T. (2012). *A study of hybrid rockets with multi-section swirl injection method*. In 48th AIAA/ASME/SAE/ASEE Joint Propulsion Conference & Exhibit (p. 3905).

Paccagnella, E., Karabeyoglu, A. M., Barato, F., & Pavarin, D. (2015). *Scaling of Hybrid Rocket Motors with Swirling Oxidizer Injection*. In 51st AIAA/SAE/ASEE Joint Propulsion Conference (p. 3833)

Parchen, R. R., & Steenbergen, W. (1998). *An experimental and numerical study of turbulent swirling pipe flows*. Journal of Fluids Engineering , 120 , 54-61.

Pope, S. B., & Pope, S. B. (2000). *Turbulent flows*. Cambridge university press.

Rocklage-Marliani, G., Schmidts, M., & Ram, V. I. V. (2003). *Three-dimensional laserdoppler velocimeter measurements in swirling turbulent pipe flow*. Flow, Turbulence and Combustion, 46, 46-67.

Roy, B. J., & Frederick, R. A. (2016). *Overview of Vortex Injected Hybrid Rocket Engines-Regression Rate Modeling*. In 52nd AIAA/SAE/ASEE Joint Propulsion Conference (p. 4530).

Smith, G. P., & Townsend, A. A. (1982). *Turbulent Couette flow between concentric cylinders at large Taylor numbers*. Journal of Fluid Mechanics, 123, 187-217.

Von Lavante, E., & Yao, J. (2012). *Numerical investigation of turbulent swirling flows in axisymmetric internal flow configurations*. Flow Measurement and Instrumentation, 25, 63-68.

White, F. M., & Corfield, I. (2006). *Viscous fluid flow* (Vol. 3, pp. 433-434). New York: McGraw-Hill.

Wilcox, D. C. (1998). *Turbulence modeling for CFD* (Vol. 2, pp. 172-180). La Canada, CA: DCW industries.

Wongyai, P., & Greatrix, D. R. (2015). *Regression rate estimation for swirling-flow hybrid rocket engines*. Journal of Propulsion and Power, 32(1), 18-22.

Yoshimura, K., & Sawada, K. (2010, January). *Numerical Simulation of Swirling Flowfield in Combustion Chamber for Hybrid Rocket Engine*. In 48th AIAA Aerospace Sciences Meeting Including the New Horizons Forum and Aerospace Exposition (p. 905).

A. Industrial Applications Examples

The propose of appendix A is to provide more examples of the swirling flow applications in the industry. Swirling flow finds applications in combustion and heat exchanger. A good example is the gas turbine engines. Figure A.1 shows a schematic of a lab-scale gas turbine combustor where a conical swirl generator with four symmetric slots injects the premixed flow into the burner. The swirling flow inside a combustion chamber results in combustion stability.

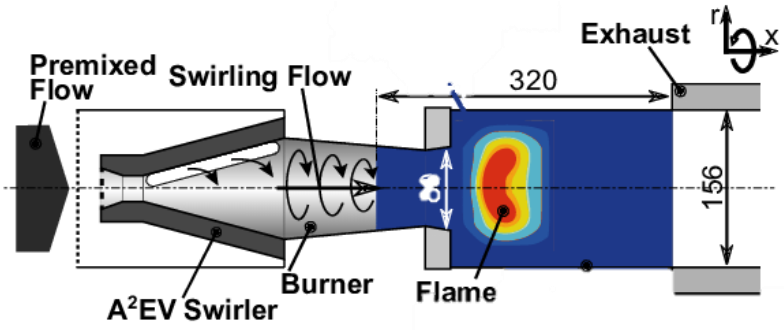

Figure A. 1 Lab-scale Gas turbine combustor (Hummel, 2016).

Another example is the industrial burners where swirling flows are widely used to increase the mixing and heat transfer rate. A schematic of an industrial swirl burner is presented in Figure A.2.

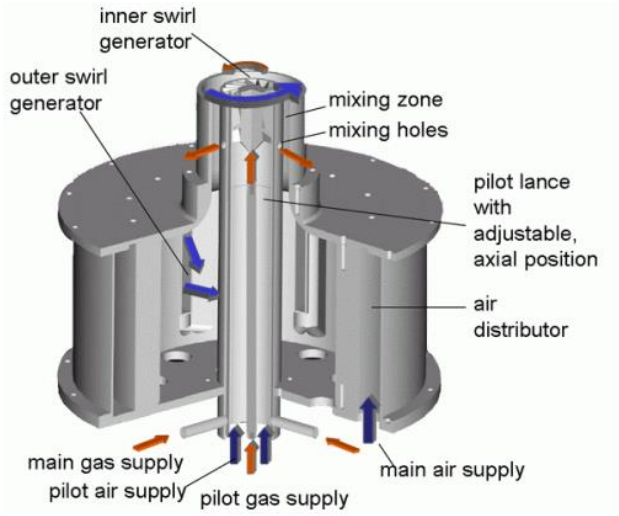

Figure A. 2 Industrial Swirl Burner (vbt.ebi.kit.edu).

The swirling flow is heavily involved in design and operation of cyclones and hydrocyclones (Figure A.3). These valuable devices are widely used in various industries such as mining and petroleum. Cyclones are mainly used to remove fine solid particles suspended in liquids or separating two liquids with different densities.

Figure A. 3 Heavy-duty Cavex hydrocyclones (Weir Minerals).

Figure A.4 shows a schematic of a hydrocyclone where the mixture is fed under

pressure and rotates around the perimeter. This swirling motion generates a low-pressure area along the axis. As a result of this low-pressure area the lighter material moves upwards and recycles to the overflow stream. Heavier material or particles on the other hand, move downward and join the underflow.

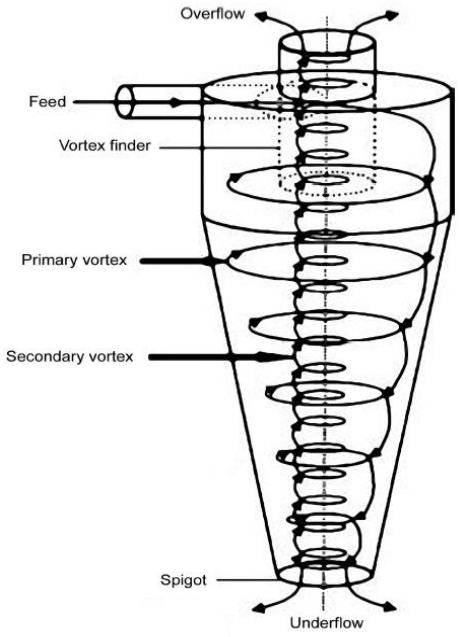

Figure A. 4 Schematic of a Hydrocyclone (Ozgen & Yildiz, 2010).

B. **Example of Highly Swirling Flow Turbulence Modeling**

The purpose of this appendix is to show the effect of the turbulence modeling in accurately solving a swirl-dominated flow through an example. Figure B.1 shows the tangential velocity profile in some location in a cyclone. The highly swirling flow field in the cyclone has been solved using different turbulence models. As it can see in the plot, the RSM predicts the flow more accurately in comparison to the other turbulence models.

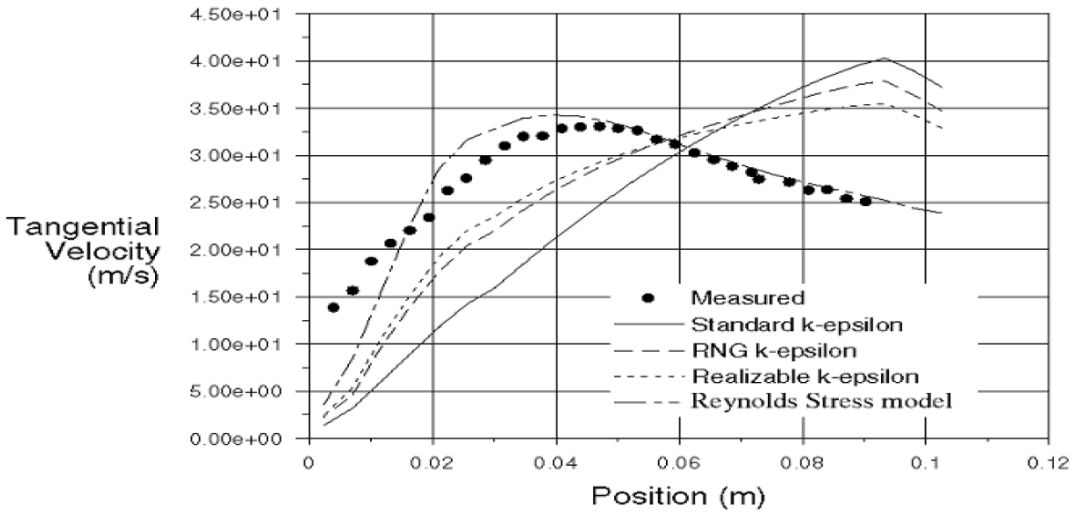

Figure B. 1 Tangential velocity profile at a location below the vortex finder (Ansys, Inc. 2013).